Computational Mechanics
https://doi.org/10.1007/s00466-025-02745-8

ORIGINAL PAPER

Coupling of peridynamics with finite elements: a case study

Anna Pernatii[1] · Danylo Filiurskyi[1] · Ulrich Gabbert[1] · Christian Willberg[2] · Jan-Timo Hesse[3]

Received: 6 June 2025 / Accepted: 30 December 2025

Abstract
The classical continuum mechanics fails in case of discontinuities. Peridynamics has been proven to be a powerful tool for solving such problems. However, it is extremely computational expensive and there are difficulties in fulfilling local boundary conditions. The paper aims to overcome these problems by coupling the Peridynamics (PD) with the Finite Element Method (FEM). Three different coupling strategies are considered in the paper: modified Schwarz Alternating Method, the Arlequin based coupling method and the Splice Method. The methods are presented and applied to one-dimensional dynamic cases, including high-frequency wave propagation analysis. The criteria applied to evaluate the methods are convergence to the local solution and difficulties choosing specific numerical parameters. The significance of long-range forces in the nature of the damage is also examined.

Keywords Peridynamics · FE-PD coupling · Wave propagation · Arlequin coupling · Schwarz coupling

1 Introduction

The solution to damage problems are particular important, especially in developing secure and reliable systems and structures. The existing damage theories can be generally divided into two groups: local and non-local approaches, depending on the range of internal forces. Local theories, like classical continuum damage mechanics [1] and its representation in the Extended Finite Element Method (XFEM) [2] often struggle in capturing long-range effects and ignore the non-local character of damage processes, which leads to inaccuracies. Non-local theories, for instance, are the cohesive zone model [3], the phase-field methods [4], the molecular dynamics approaches [5] etc. However, applying the cohesive zone model assumes that the crack path is known in advance at the current state, which is usually not the case, especially in analyzing highly dynamic crack propagation in complex system configurations. There are some applications of molecular dynamics [6] to investigate the fracture processes. For this purpose, the body should either be represented by millions of atoms to model a structure with properly large dimensions or should be up-scaled to a lower-resolution model [7]. Also, non-local models are mesh-sensitive and require much higher resolution than regular approaches. This increases the computational efforts significantly.

Peridynamics has emerged as an effective theory for studying dynamic fracture problems. Here, internal forces are represented by non-local interactions that occur between pairs of material points distributed throughout a continuous body. The radius of the non-local neighborhood defines the grade of non-locality, called the horizon δ. After the first publication of Silling [8] regarding peridynamics, the theory has experienced significant improvement. The state-based peridynamics [9] was introduced as a reformulation of bond-based peridynamics to address limitations related to Poisson's ratio. In this formulation, the term "state" replaces "bond," emphasizing that the response of a material point depends on the deformation of all the bonds associated with it. The peridynamic theory has already found a wide range of applications. It enables the simulation of crack initiation and its propagation, providing an accurate

✉ Anna Pernatii
apernatiy@gmail.com

[1] Institute of Materials, Technologies and Mechanics, Otto-von-Guericke University Magdeburg, Universitaetspl. 2, 39106 Magdeburg, Germany

[2] Institute of Engineering and Industrial Design, Magdeburg-Stendal University of Applied Sciences, Breitscheidstr. 2, 39114 Magdeburg, Germany

[3] Present address: Institute of Lightweigth Systems, German Aerospace Center (DLR), Lilienthalpl. 7, 38108 Braunschweig, Germany

Published online: 22 January 2026

result for the crack propagation speed [10]. Furthermore, peridynamics can also handle the simulation of damage processes in composites, such as delamination [11], matrix cracking [12], fibre-matrix debond and matrix failure [13], that could be used in aerospace and civil engineering materials research. The theory could also yield accurate results for high-velocity impact and penetration problems, which could later be applied in defense and aerospace engineering, as seen in [14, 15], and [16]. Moreover, frameworks have been developed for analyzing additive manufacturing processes [17] as well as the damage issues arising from them [18]. Additionally, peridynamics has been utilized in coupled formulations for multi-field problems, such as heat transfer [19], diffusion [20] and electronics [21]. One can observe the application of peridynamics to micromechanical problems. The homogenization modeling provided by [22] and [23] shows the potential of peridynamics on the micro-level through peridynamic micro–macro correspondence schemes. The detailed examination of thin films peeling [24] shows the non-local response of the peeled layer, offering valuable insights for investigating adhesive joints and determining critical peeling forces. While peridynamics demands less computational effort than some damage theories, which give similar accuracy regarding fracture, the processing time is still less efficient compared to classical computational methods.

FEM theory is wide-used in structural mechanics, but has limitations by dealing with fractures. The approach uses the partial differential equation to describe the relationship between external loads b, inertia loads $\rho\ddot{\mathrm{u}}$, and the forces in the body, where the mechanical stresses $\boldsymbol{\sigma}$ are determined by spatial derivatives of the displacements u. As the derivative at the crack tip is not defined, one can define a critical stress value and after that switch to the classical fracture mechanics [7]. A coupling of PD and FEM may have good potential in solving dynamic fracture problems and overcoming the disadvantages of both methods at the same time. The damage-free domain is supposed to be modeled with FEM, while a zone where the damage is presented or expected is modeled through PD points. This could lead to a decreasing of computational time without loss of accuracy. The Splice Method [25] can be mentioned among existing coupling methods. The coupling is achieved by considering that peridynamic points can "see" through a horizon δ finite elements, and these connections are enough to achieve a coupling. Because of the relative simplicity of implementation, there is also the possibility of developing a multi-adaptive approach [26] with an adaptive changing interface between the domains dependent on crack growth. Another method proposes to bridge two subdomains by introducing a special transition element [27]. Such direct coupling leads to deviations, as shown in the results. The partitioning procedure by using, for example, the Schwarz method [28] is a relatively simple and efficient technique. The main advantage is that it allows to couple two black-box solvers by defining constraints on the common interface.

The approach presented in [29], proposes to achieve the coupling by force blending in the overlapping area. The implemented method is presented in 1D static cases. Nevertheless, a noticeable error is present. A similar idea is demonstrated by the morphing strategy [30] to couple local and non-local methods. The coupling is performed through a transition region, where the gradient of the material parameters is defined by a morphing function.

Some methods ensure the mechanical compatibility of domains of different nature on the energy scale. Among them are the Arlequin Method [31], its adaptation for coupling of Classical Elasticity (CE) and PD [32] and further developments [33, 34] in considering the static and dynamic cases and wave propagation problems. The quasi-nonlocal method [35] is also an energy-based approach that reconstructs the non-local interactions for a subregion with local interactions for 1D problems. However, the technique is difficult to apply for higher dimensional cases. Its improvement [36] proposes a reconstructed energy functional with a modified elasticity tensor, which allows the specification of the range of validity of non-local forces. The multiscale method by [37] combines bridging scale and perfectly matched layer approaches to eliminate artificial reflections and reduce impedance at the interface. Another coupling method [38] between PD and numerical substructure method integrates PD part by using interface elements with embedded PD nodes.

The present paper studies three coupling techniques: the Schwarz Method, the Arlequin Approach and the Splice Method. They have already been shown to be efficient for static cases, and the research goal is to investigate their performance for highly dynamic problems. The structure of this paper is as follows: Sect. 2 presents the theoretical review of the finite element method and the peridynamic theory. Also it gives an overview to elastic wave characteristic in both continuum mechanics and in peridynamics. Section 3 is dedicated to detailed characterization of the coupling methods. The 1D implementation of all coupling approaches, parameter studies, and dynamic tests are presented in Sect. 4. Finally, the concluding remarks are given in Sect. 5.

2 Materials and methods

2.1 Continuum mechanics and FEM

The FEM is the most widely used method for the simulation of structural problems in engineering. A distinctive feature of the finite element method is the division of a given domain into a set of simple subdomains, called finite elements [39]. For arbitrary problems it is not possible to find functions to describe the solution of the whole domain as in the Ritz method [40].

Following [41] the dynamic equations of a continuum can be derived using *Hamilton*s principle, which states that the motion of the system in the time interval $[t_1,\, t_2]$ is such that the variation of the action vanishes, i.e. the motion of the system takes the path of stationary action as

$$\delta \int_{t_1}^{t_2} (L + W)\, \mathrm{dt} = 0\,, \tag{1}$$

where L represents the *Lagrangian*, and W the work of the external forces. The *Hamilton*s principle is adapted in a way that the *Lagrangian* includes in the mechanical case the kinetic energy and the potential energy and can be determined as

$$L = \int_V \frac{1}{2} \left[\rho \dot{\mathrm{u}}^T \dot{\mathrm{u}} - \boldsymbol{\varepsilon}^T \boldsymbol{\sigma}\right]\, \mathrm{dV}\,, \tag{2}$$

with the mass density ρ and the velocity field $\dot{\mathrm{u}}$. The external work W done by external mechanical forces f related to volumes $(..)_V$, surfaces $(..)_{S_i}$ and nodals $(..)_i$ is given as

$$W = \int_V \mathrm{u}^T \mathrm{f}_V\, \mathrm{dV} + \int_{S_1} \mathrm{u}^T \mathrm{f}_{S_1}\, \mathrm{dS}_1 + \sum_{i=1}^{n} \mathrm{u}_i^T \mathrm{f}_i\,. \tag{3}$$

With *Hooke*'s law

$$\boldsymbol{\sigma} = \mathrm{C}^E \boldsymbol{\varepsilon} \tag{4}$$

and substituting the Equations (2) and (3) in Equation (1) the *Hamilton*s principle is obtained in the following form

$$0 = -\int_V \left[\rho \delta \mathrm{u}^T \ddot{\mathrm{u}} + \delta \boldsymbol{\varepsilon}^T \mathrm{C}^E \boldsymbol{\varepsilon}\right]\, \mathrm{dV} + \int_V \delta \mathrm{u}^T \mathrm{f}_V\, \mathrm{dV} + \int_{S_1} \delta \mathrm{u}^T \mathrm{f}_{S_1}\, \mathrm{dS}_1 + \sum_{i=1}^{n} \delta \mathrm{u}_i^T \mathrm{f}_i, \tag{5}$$

where $\ddot{\mathrm{u}}$ is the acceleration. Based on Equation (5) the finite element equations can be derived. When using the finite element approach a continuous body is approximated with shape functions defined on a local domain (elements). The displacements $\mathrm{u}^{(m)}$ in an element can be expressed as

$$\mathrm{u}^{(m)}(\mathrm{x}) = \mathrm{N}_u^{(m)}(\mathrm{x})\mathrm{u}_\mathrm{N}. \tag{6}$$

$\mathrm{N}^{(m)}$ is an interpolation matrix which includes the shape functions. u_N is the displacement vector, m is the element number and $\mathrm{x} = [x_1,\, x_2,\, x_3]$ is the position vector [40]. The mechanical strain is defined as $\boldsymbol{\varepsilon} = \boldsymbol{\mathcal{D}}\mathrm{u}$, where $\boldsymbol{\mathcal{D}}$ is the differential operator. With Equation (6) the element strain can be derived directly as

$$\boldsymbol{\varepsilon}^{(m)}(\mathrm{x}) = \boldsymbol{\mathcal{D}}\mathrm{N}_u^{(m)}(\mathrm{x})\mathrm{u}_\mathrm{N} = \mathrm{B}_u^{(m)}(\mathrm{x})\mathrm{u}_\mathrm{N}. \tag{7}$$

If the approximation of the mechanical displacements Equation (6) and the strains Equation (7) is substituted in Equation (5) the equations are obtained as

$$\begin{aligned} &\delta \mathrm{u}_\mathrm{N}^T \int_V \mathrm{N}_u^{(m)T} \rho \mathrm{N}_u^{(m)} \mathrm{dV} \ddot{\mathrm{u}}_\mathrm{N} + \delta \mathrm{u}_\mathrm{N}^T \int_V \mathrm{B}_u^{(m)T} \mathrm{C}^E \mathrm{B}_u^{(m)} \mathrm{dV} \mathrm{u}_\mathrm{N} \\ &= \delta \mathrm{u}_\mathrm{N}^T \int_V \mathrm{N}_u^{(m)T} \mathrm{F}_V \mathrm{dV} + \delta \mathrm{u}_\mathrm{N}^T \int_{S_1} \mathrm{N}_u^{(m)T} \mathrm{F}_{S_1} \mathrm{dS}_1 + \delta \mathrm{u}_\mathrm{N}^T \mathrm{N}_u^{(m)T} \mathrm{F}_P\,. \end{aligned} \tag{8}$$

Equation (8) is valid for any arbitrary variation of the displacements $\delta \mathrm{u}_\mathrm{N}$ and thus yields

$$\mathrm{M}\ddot{\mathrm{u}}_\mathrm{N} + \mathrm{K}\mathrm{u}_\mathrm{N} = \mathrm{f}_\mathrm{ext}\,. \tag{9}$$

The abbreviations in common use are the mass matrix M, the stiffness matrix K and the vector of the external mechanical forces f_ext.

In this paper a 1D problem is studied and the matrices for one element are given as

$$\mathrm{M}^{(m)} = \frac{\rho A^{(m)} L^{(m)}}{2} \begin{bmatrix} 1 & 0 \\ 0 & 1 \end{bmatrix} \quad \text{and} \quad \mathrm{K}^{(m)} = \frac{A^{(m)} E^{(m)}}{L^{(m)}} \begin{bmatrix} 1 & -1 \\ -1 & 1 \end{bmatrix}. \tag{10}$$

Let $L^{(m)}$ the element length, $A^{(m)}$ the truss cross-section area and $E^{(m)}$ the Young's modulus be the same for all elements. The lumped mass matrix is given in a diagonalized form. Then, the whole finite element system of equation can be determined by assuming that all elements have an equal size with the length L and the sum of all nodal element forces is equal to the external force. The system matrices for constant properties are given as

$$\mathbf{M} = \frac{\rho AL}{2}\begin{bmatrix} 1 & 0 & \cdots & 0 & 0 \\ 0 & 2 & & & \\ \vdots & & \ddots & & \\ & & & 2 & 0 \\ 0 & 0 & \cdots & 0 & 1 \end{bmatrix} \text{ and}$$
$$\mathbf{K} = \frac{AE}{L}\begin{bmatrix} 1 & -1 & \cdots & 0 & 0 \\ -1 & 2 & & & \\ \vdots & & \ddots & & \\ & & & 2 & -1 \\ 0 & 0 & \cdots & -1 & 1 \end{bmatrix}. \tag{11}$$

2.2 Peridynamics

The paper follows the assumptions and notations from [42]. Within the neighborhood $\mathcal{H}$, with the volume V_{x}, defined by a spherical domain the horizon δ, the force volume density state $\underline{\mathrm{T}}$ for the bond interaction between the positions x and x' is defined as the integral balance of momentum

$$\int_{\mathcal{H}} (\underline{\mathrm{T}}(\mathrm{x},t)\langle \mathrm{x}' - \mathrm{x}\rangle - \underline{\mathrm{T}}(\mathrm{x}',t)\langle \mathrm{x} - \mathrm{x}'\rangle)\mathrm{d}V_{\mathrm{x}} + \mathrm{b} = \rho\ddot{\mathrm{u}}. \tag{12}$$

Three variations of the peridynamic model are currently being used, the Bond-based (BB), the Ordinary state-based (OSB) and also the Non-ordinary state-based (NOSB) formulation. In this order, flexibility increases, but so does also the complexity of the formulations. In this paper the focus is on BB, which can be interpreted as a non-local spring formulation.

The equation of motion for the initially introduced BB peridynamic theory is defined by

$$\rho(\mathrm{x})\ddot{\mathrm{u}}(\mathrm{x},t) = \int_{\mathcal{H}_{\mathrm{x}}} \mathrm{f}_{\mathrm{bond}}\,(\mathrm{x'},\mathrm{x},t)\; \mathrm{d}V_{H_{\mathrm{x}}} + \mathrm{b}(\mathrm{x},t), \tag{13}$$

where $\mathrm{f}_{\mathrm{bond}}(\mathrm{x'},\mathrm{x},t) = -\mathrm{f}_{\mathrm{bond}}(\mathrm{x},\mathrm{x'},t)$ is a pairwise force function which represents the force that x' exerts on x. In order to assure the conservation of linear momentum, the pairwise force function is anti-symmetric, [43]. The pairwise force function can be split into the two bond force densities $\mathrm{f}(\mathrm{x'},\mathrm{x},t)$ and $\mathrm{f}(\mathrm{x},\mathrm{x'},t)$ as

$$\mathrm{f}_{\mathrm{bond}}(\mathrm{x'},\mathrm{x},t) = \mathrm{f}(\mathrm{x},\mathrm{x'},t) - \mathrm{f}(\mathrm{x'},\mathrm{x},t), \tag{14}$$

with

$$\begin{aligned}\mathrm{f}(\mathrm{x},\mathrm{x'},t) =& \frac{1}{2}\mathrm{f}_{\mathrm{bond}}(\mathrm{x'},\mathrm{x},t) \quad \text{and} \quad \mathrm{f}(\mathrm{x'},\mathrm{x},t) \\ =& -\frac{1}{2}\mathrm{f}_{\mathrm{bond}}(\mathrm{x'},\mathrm{x},t).\end{aligned} \tag{15}$$

Thus, the bond force densities are equal in magnitude but opposite in direction. This is a crucial factor in the bond-based theory. Both bond force densities can be expressed as force vector states $\mathrm{f}(\mathrm{x},\mathrm{x'},t) = \underline{\mathrm{T}}(\mathrm{x'},t)\,\langle \mathrm{x} - \mathrm{x'}\rangle$ and $\mathrm{f}(\mathrm{x'},\mathrm{x},t) = \underline{\mathrm{T}}(\mathrm{x},t)\,\langle \mathrm{x'} - \mathrm{x}\rangle$. In order to incorporate the properties that are crucial for bond-based peridynamics, the force vector states are chosen of the form

$$\begin{aligned}\underline{\mathrm{T}}(\mathrm{x'},t)\,\langle \mathrm{x} - \mathrm{x'}\rangle =& \frac{1}{2}C(\xi)\frac{\mathrm{y'} - \mathrm{y}}{|\mathrm{y'} - \mathrm{y}|} \quad \text{and} \quad \underline{\mathrm{T}}(\mathrm{x},t)\,\langle \mathrm{x'} - \mathrm{x}\rangle \\ =& -\frac{1}{2}C(\xi)\frac{\mathrm{y'} - \mathrm{y}}{|\mathrm{y'} - \mathrm{y}|}.\end{aligned} \tag{16}$$

Both force vector states are parallel to the relative position vector of the material points in the deformed configuration. Therefore the balance of angular momentum is satisfied [42].

The micromodulus $C(\xi)$ in Equation (16) relates the bond force to the bond stretch $s(\mathrm{y'} - \mathrm{y}, \mathrm{x'} - \mathrm{x})$ [44]. As introduced in [43], the parameter can be chosen linearly dependent on the stretch in the form $C(\xi) = cs(\mathrm{y'} - \mathrm{y}, \mathrm{x'} - \mathrm{x})$. Here the constant c is a PD material parameter and s is defined as follows:

$$s = \frac{|\mathrm{y'} - \mathrm{y}| - |\mathrm{x'} - \mathrm{x}|}{|\mathrm{x'} - \mathrm{x}|}.$$

Thus, the force states in the bond-based theory can be expressed in the form

$$\begin{aligned}\underline{\mathrm{T}}(\mathrm{x'},t)\,\langle \mathrm{x} - \mathrm{x'}\rangle =& \frac{1}{2}cs\frac{\mathrm{y'} - \mathrm{y}}{|\mathrm{y'} - \mathrm{y}|} \quad \text{and} \quad \underline{\mathrm{T}}(\mathrm{x},t)\,\langle \mathrm{x'} - \mathrm{x}\rangle \\ =& -\frac{1}{2}cs\frac{\mathrm{y'} - \mathrm{y}}{|\mathrm{y'} - \mathrm{y}|}.\end{aligned} \tag{17}$$

The limitation of BBPD is that the Poisson's ratio is limited in plane strain to $\frac{1}{4}$ and for 3D and plane stress to $\frac{1}{3}$ [45]. The constant c is defined [46] as

$$c_{1D} = \frac{2E}{A\delta^2}; \tag{18}$$

$$c_{2D-plstrs} = \frac{6E}{(1-2\nu)\pi h\delta^3}, \quad c_{2D-plstrn} = \frac{6E}{(1+\nu)(1-2\nu)\pi h\delta^3}; \tag{19}$$

$$c_{3D} = \frac{6E}{(1-2\nu)\pi\delta^4}; \tag{20}$$

where A is the area, h the thickness, ν the Poisson's ratio and E the Young's modulus.

2.3 Wave equation and characteristic

2.3.1 Elastic waves in classical elasticity

Assuming small deflections, the one-dimensional governing equation of a string in classical elasticity has the form [47]:

$$\frac{\partial^2 \mathrm{u}}{\partial t^2} = \frac{1}{v^2}\frac{\partial^2 \mathrm{u}}{\partial \mathrm{x}^2}, \tag{21}$$

where v^2 represents a phase velocity constant, that for longitudinal and transversal cases can be found as follows: $v_L^2 = \frac{\lambda+2\mu}{\rho}$ and $v_T^2 = \frac{\mu}{\rho}$, with λ and μ as Lame parameters. It is assumed that the wave propagates in a positive direction without distortion. Let's consider an expression for the longitudinal displacement of the form:

$$\mathrm{u}(\mathrm{x}, t) = Ae^{ik(\mathrm{x}-vt)}, \tag{22}$$

with wave amplitude A, that is independent of x and t. The argument $k(\mathrm{x} - vt)$ is a phase of the wave. If $\mathrm{u}(\mathrm{x}, t)$ is periodic with wavelength Λ, then $\Lambda = \frac{2\pi}{k}$, where k counts the number of wavelength over the period 2π. The circular frequency is expressed as $\omega = kv$, which follows from the representation of $\mathrm{u}(\mathrm{x}, t)$. Phase velocity is detected from the particle velocity and the maximum value of the ratio between u and v be expressed as: $(\frac{\dot{\mathrm{u}}(\mathrm{x},t)}{v_L})_{\max} = Ak = 2\pi A/\Lambda$ and $A/\Lambda \ll 1$.

In linear continuum mechanics, the phase velocities of traveling harmonic waves in 1D are independent of the wavelength Λ. This means that short and long waves propagate with the same phase velocity, leading to the system's nondispersive properties [48].

2.3.2 Elastic waves in bond-based peridynamics

If the system shows inelastic properties or nonlocality, the dispersed behavior emerges. Consider a nonlocal 1D peridynamic string and define a variable ξ as a vector between two points inside the horizon: $\xi = \mathrm{x}' - \mathrm{x}$. If small deformations are assumed, the equation of motion is reduced to the following form:

$$\rho\ddot{\mathrm{u}}(\mathrm{x}, t) = \int_{-\delta}^{+\delta} C(\xi)\frac{\mathrm{u}(\mathrm{x}+\xi) - \mathrm{u}(\mathrm{x})}{|\xi|}\mathrm{d}\xi + b(\mathrm{x}, t). \tag{23}$$

$C(\xi)$ is a micromodulus. Following [49] and substituting Equation (22) into Equation (23) it results in:

$$A\rho i^2 k^2 v^2 e^{ik(\mathrm{x}-vt)} = \int_{-\delta}^{+\delta} \frac{C(\xi)}{|\xi|} Ae^{ik(\mathrm{x}-vt)}(e^{ik\xi} - 1)\mathrm{d}\xi + b(\mathrm{x}, t) \tag{24}$$

Taking into account, that i is an imaginary unit and that time and amplitude can be eliminated, the previous equation is reduced to:

$$-\rho k^2 v^2 = \int_{-\delta}^{+\delta} \frac{C(\xi)}{|\xi|}(\cos(k\xi) - 1)\mathrm{d}\xi + i\int_{-\delta}^{+\delta} \frac{C(\xi)}{|\xi|}\sin(k\xi)\,\mathrm{d}\xi. \tag{25}$$

The last integral is equal to zero, since $\sin k\xi$ is an odd function, therefore:

$$\begin{aligned} v^2 =& \frac{2}{\rho k^2}\int_0^{\delta} C(\xi)\frac{1-\cos(k\xi)}{\xi}\mathrm{d}\xi \approx \frac{2}{\rho k^2}\int_0^{\delta} C(\xi)\frac{k^2\xi^2}{2\xi}\mathrm{d}\xi \\ =& \frac{1}{\rho}\int_0^{\delta} C(\xi)\xi\mathrm{d}\xi \end{aligned} \tag{26}$$

It should be mentioned that the $\cos(k\xi)$ function was approximated by $1 - (k\xi)^2/2$ from Taylor's expansion. Moreover, the result corresponds to Young's modulus in elasticity since $E = 1/2\int_{\mathcal{H}} C(\xi)|\xi|\mathrm{d}\xi$ [49]. The limit of the expression by $\delta \longrightarrow 0$ corresponds to the classical case where $v = \sqrt{\frac{E}{\rho}}$. Another different examples of micromodulus functions and their influence on elastic behavior were shown in [50–52]. However, in the present work, it is considered a uniform micromodulus $C(\xi) = \bar{c}$. To determine the relation of phase velocity to the horizon in bond-based PD the Equation (26) is evaluated as follows:

$$\left(\frac{v}{v_0}\right)^2 = \frac{4}{(k\delta)^2}\int_0^{\delta}\frac{1-\cos(k\xi)}{\xi}\mathrm{d}\xi \quad \text{where} \quad v_0^2 = \frac{\bar{c}\delta^2}{2\rho} \tag{27}$$

Thus, Fig. 1 displays the relation of normed phase velocity to the ratio $k\delta/2\pi$, which can be interpreted as a function of the number of wavelengths per horizon. Since the previous equation gives the phase's velocity in the square, the solution of the equation has positive and negative roots. The Fig. 1 shows the result with a positive root.

3 Coupling methods

3.1 Schwarz approach

The Schwarz domain decomposition is one of the oldest domain decomposition methods, which was invented by Hermann Amandus Schwarz in 1869. Since that time various extensions and adaptations of this technique emerged. These methods include, among others, The Schwarz Alternating Method, and the Parallel Schwarz Method [53], the Discrete Schwarz methods, the Additive Schwarz Method, and also different types of optimized Schwarz methods [54]. In the paper at hand, our primary focus is on the Schwarz Alternating Method.

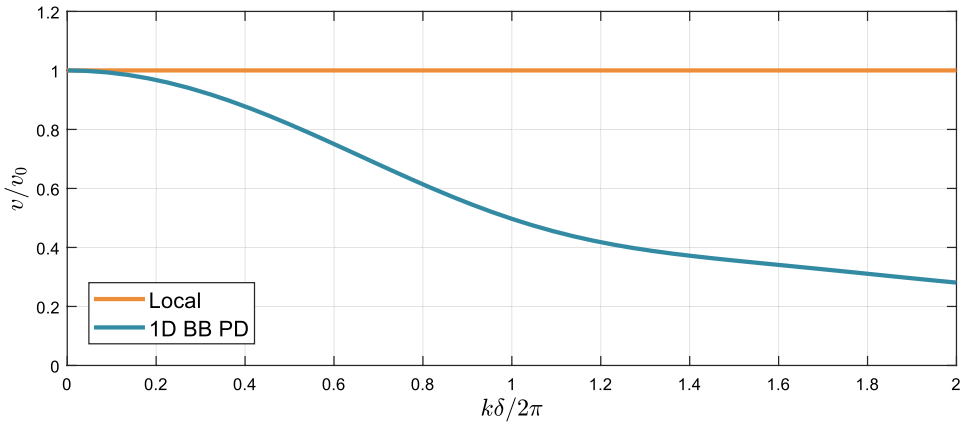

Fig. 1 Phase velocity for wave propagation in one-dimensional bond-based peridynamics vs in classical elasticity

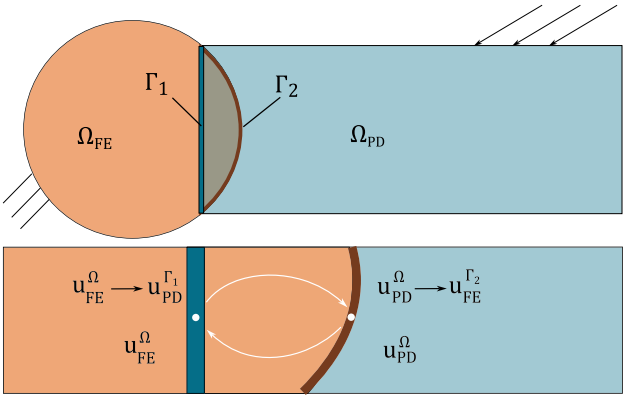

Fig. 2 Domain decomposition in Schwarz Alternating Method with information exchange through the boundaries Γ_1 and Γ_2. The choice of boundary size is discussed in Sect. 4

This approach is chosen for its intuitive usability and its documented linear convergence, as indicated by [55]. The method presents a fundamental idea for solving complex problems by decomposing the whole domain into two or more domains with some overlap. The solution is based on an algorithm that solves the problem in one domain and then moves to the next one, using the results of the previous iteration, and so on.

The general solution algorithm is illustrated in Fig. 2. In the following the coupling approach is presented for a one-dimensional elasto-dynamic problem. One subdomain corresponds to a domain calculated with classical theory, while the remaining part corresponds to a subdomain, calculated using Peridynamic theory.

The entire domain is denoted as $\Omega \subset \mathrm{R}^1$. The first subdomain is referred to as the Finite Element (FE) domain, denoted as Ω_{FE}, while the second one concerns to the PD domain, labeled as Ω_{PD}. The intersection of these two subdomains, which serves as the overlap between the FE and PD sections, is given as $\Omega_o = \Omega_{\mathrm{FE}} \cap \Omega_{\mathrm{PD}}$.

In the following the coupling procedure is presented in detail. Both frameworks are coupled in a partitioned approach, which means that they communicate and exchange information just through the common boundaries. For the transition region, only Dirichlet boundary conditions are considered, meaning that only the displacement is to be transferred from one subdomain to another. Using the notation of the interfaces $\Gamma_1 = \partial\Omega_{\mathrm{FE}} \cap \Omega_{\mathrm{PD}}$ and $\Gamma_2 = \partial\Omega_{\mathrm{PD}} \cap \Omega_{\mathrm{FE}}$, where $\partial\Omega$ stands for the external boundary of the corresponding region, the general algorithm of the Schwarz Alternating Method can be shown as follows:

1. Set an initial displacement value $\mathrm{u}^{\Gamma_2}_{\mathrm{FE}}$ on the boundary and solve for the subdomain with FE:

$$\mathrm{M}\ddot{\mathrm{u}}^n_{\mathrm{FE}}(\mathrm{x}) + \mathrm{K}\mathrm{u}^n_{\mathrm{FE}}(\mathrm{x}) = \mathrm{F}^n_{\mathrm{FE}}, \quad \forall \mathrm{x} \in \Omega_{\mathrm{FE}}.$$

2. Transition between two different regions occurs by finding the value:

$$\mathrm{u}^n_{\mathrm{FE}}(\mathrm{x}) \longrightarrow \mathrm{u}^n_{\mathrm{PD}}(\mathrm{x}), \quad \forall\, \mathrm{x} \in \Gamma_1.$$

3. With obtained displacement values on the boundary find the solution for the second PD subdomain Ω_{PD}:

$$\rho\ddot{\mathrm{u}}^n_{\mathrm{PD}}(\mathrm{x}) = \sum_{\mathrm{PD}} \left(c_i\, s_i\, \frac{\mathrm{y'} - \mathrm{y}}{|\mathrm{y'} - \mathrm{y}|} V_i \right)^n + \mathrm{b}^n_{\mathrm{PD}}, \quad \forall\, \mathrm{x} \in \Omega_{\mathrm{PD}} \notin \Gamma_1.$$

4. Similar to the step before find the displacement value on Γ_2 and pass it to the another subdomain:

$$\mathrm{u}^n_{\mathrm{PD}}(\mathrm{x}) \longrightarrow \mathrm{u}^n_{\mathrm{FE}}(\mathrm{x}), \quad \forall\, \mathrm{x} \in \Gamma_2.$$

5. Find the solution for the domain Ω_{FE}:

$$\mathrm{M}\ddot{\mathrm{u}}^n_{\mathrm{FE}}(\mathrm{x}) + \mathrm{K}\mathrm{u}^n_{\mathrm{FE}}(\mathrm{x}) = \mathrm{F}^n_{\mathrm{FE}}, \quad \forall\, \mathrm{x} \in \Omega_{\mathrm{FE}} \notin \Gamma_2.$$

6. Check whether the convergence is reached, where ε is a predefined parameter:

$$\mathrm{u}^n_{\mathrm{FE}}(\mathrm{x}) - \mathrm{u}^n_{\mathrm{PD}}(\mathrm{x}) \leq \varepsilon, \quad \forall\, \mathrm{x} \in \Gamma_2.$$

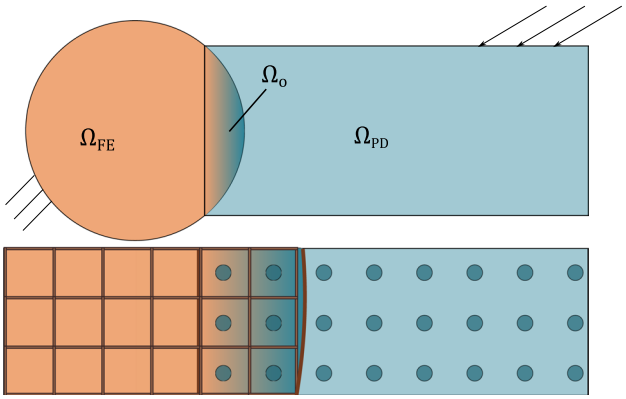

Fig. 3 Domain decomposition in Arlequin Coupling method with overlapping region, where the properties are weighted, dependent on a function $\alpha(\mathrm{x})$

7. If yes, go to the next time step $n = n + 1$.

3.2 Arlequin approach

The Arlequin Method is a computational technique that can be used to bridge the gap between atomistic and continuum theories in the context of modeling damage problems. The main idea of the coupling [56] consist on the assumption that the energy in the coupling region is distributed by using a weighting function whose sums are equal to unity to conserve the local mechanical energies. In the overlapping area domains are glued to each other to reach the proper material behavior.

Let the general domain be divided into two sub-domains that overlap (Fig. 3). The size of the overlapping region is discussed below.

Let the sum of energies are written as bellow:

$$\begin{aligned}\mathcal{H}_{\mathrm{tot}}(\mathrm{u_{FE}}, \dot{\mathrm{u}}_{\mathrm{FE}}, \mathrm{u_{PD}}, \dot{\mathrm{u}}_{\mathrm{PD}}) =& \alpha(\mathrm{x})\mathcal{H}_{\mathrm{FE}}(\mathrm{u_{FE}}, \dot{\mathrm{u}}_{\mathrm{FE}}) \\ &+ (1-\alpha(\mathrm{x}))\mathcal{H}_{\mathrm{PD}}(\mathrm{u_{PD}}, \dot{\mathrm{u}}_{\mathrm{PD}}).\end{aligned} \tag{28}$$

The interface between domains should be well-balanced. Thus the choice of weighting function $\alpha(\mathrm{x})$ [57] (Fig. 4) can influence a material response in the coupling zone and play a crucial role in determining how information is exchanged between different models. Moreover, it is assumed that $\alpha(\mathrm{x})$ is a positive piece-wise continuous function satisfying the following conditions:

$$\alpha(\mathrm{x}) = \begin{cases} 1 & \forall \mathrm{x} \in \Omega_{\mathrm{FE}} \cap \Omega_o, \\ 0 & \forall \mathrm{x} \in \Omega_{\mathrm{PD}} \cap \Omega_o, \\ \alpha(\mathbf{x_o}) & \forall \mathrm{x} \in \Omega_o, \end{cases} \tag{29}$$

From the energy conservation principle, we can depict the total mechanical energy as sum of energies that is valid for both the classical elasticity and the peridynamic theory:

$$\mathcal{H}_{\mathrm{tot}} = \mathcal{W}^{\mathrm{kin}} + \mathcal{W}^{\mathrm{int}} - \mathcal{W}^{\mathrm{ext}}. \tag{30}$$

From the first form of Hamilton's principle for conservative systems, mentioned in Equation (1), a kinetic energy of a moving system for both CE and PD can be expressed as follows:

$$\begin{aligned}\mathcal{W}^{\mathrm{kin}}_{\mathrm{FE}} &= \mathrm{M}\dot{\mathrm{u}}^2_{\mathrm{FE}}/2 \\ \mathcal{W}^{\mathrm{kin}}_{\mathrm{PD}} &= \rho V_{\Omega_{\mathrm{PD}}}\dot{\mathrm{u}}^2_{\mathrm{PD}}/2\end{aligned} \tag{31}$$

The internal energy, which is the work done by the internal forces has the form:

$$\begin{aligned}\mathcal{W}^{\mathrm{int}}_{\mathrm{FE}} &= \frac{1}{2}\int_{\Omega_{\mathrm{FE}}} \boldsymbol{\varepsilon} : \boldsymbol{\sigma} d\Omega \\ \mathcal{W}^{\mathrm{int}}_{\mathrm{PD}} &= \mathrm{f}(\boldsymbol{\eta}, \boldsymbol{\xi}) V_{\Omega_{\mathrm{PD}}}\end{aligned} \tag{32}$$

And the work done by external forces can be calculated as follows:

$$\begin{aligned}\mathcal{W}^{\mathrm{ext}}_{\mathrm{FE}} &= \int_{\Omega_{\mathrm{FE}}} \mathrm{u}\rho\mathrm{b}d\Omega \\ \mathcal{W}^{\mathrm{ext}}_{\mathrm{PD}} &= \mathrm{u_{PD}} \mathrm{b} V_{\Omega_{\mathrm{PD}}}\end{aligned} \tag{33}$$

Using displacements as the primary variable, we derive the system of equations of motion from the system of energy equations. More details can be found in [33].

To achieve compatibility between the two regions, additional constrains should be considered in the overlapping

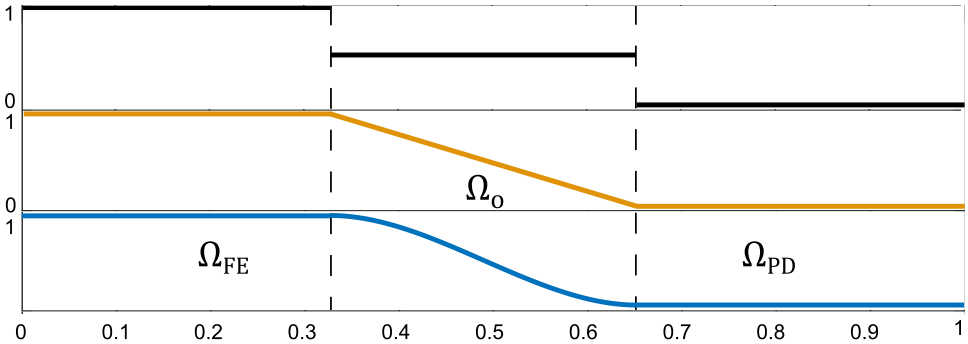

Fig. 4 Different weighting functions $\alpha(\mathrm{x})$; top - piecewise constant; middle - piecewise linear; bottom - piecewise cubic

area. In the present study, we focus on the implementation of the penalty-based Arlequin method.

The first step in achieving mechanical compatibility is to ensure that the difference in the displacements are zero. So consider the classical elasticity domain which is represented through finite elements and the second region is descretized using the meshfree PD method.

Let a set of constraint equations in the general case $\mathrm{z(u)}$ consist of the displacement-dependent term Zu and a constant term $\mathrm{z_0}$, which are always positive or zero, so that:

$$\mathrm{z(u) = z_0 + Zu = 0.} \tag{34}$$

This equation is fulfilled when the constraints are satisfied and the variation of a product reaches its minimum [40]:

$$\delta(\mathrm{z(u)^T z(u)}) = 0. \tag{35}$$

This results in the new functional:

$$\Xi = L(\mathrm{x,u},t) + \frac{1}{2}\kappa \int_{\Omega_o} \mathrm{z}^T \mathrm{z d}\Omega_o \rightarrow \mathrm{Min}, \tag{36}$$

where $L(\mathrm{x,u},t)$ is Lagrangian of the dynamic system and the term κ is the "penalty parameter" that should also be a positive and a large enough number. However, in the Arlequin framework it should be restricted to avoid negating the energy partitioning effect. The solution will satisfy the constrains only approximately depending on the selection of the penalty term. The integral is calculated only in the coupling area and solved points-wise [58]. It is assumed that the reference PD points in the overlap domain are given, and each of them should be coupled with a corresponding finite element. Then the functional in (36) has the form:

$$\Xi = \frac{1}{2}\dot{\mathrm{u}}^T \mathrm{M}\dot{\mathrm{u}} + \frac{1}{2}\mathrm{u}^T \mathrm{K u} - \mathrm{u}^T \mathrm{F} + \frac{1}{2}\kappa(\mathrm{z_0 + Zu})^T(\mathrm{z_0 + Zu}). \tag{37}$$

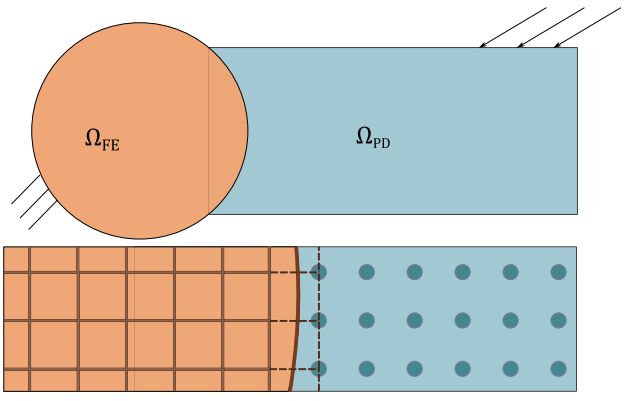

Fig. 5 Schematic illustration of Splice Coupling Method. Coupling between FE and PD domains is occurred through coupled elements in the interface and bonds, that connects PD points and FE nodes

In order to minimize the functional Ξ, the partial derivative should be calculated as:

$$\frac{\partial \Xi}{\partial \mathrm{u}} = 0, \quad \rightarrow \quad \mathrm{M\ddot{u} + (K + K_z)u = F - F_z;}$$

$$\mathrm{K_z = \kappa Z^T Z;}$$

$$\mathrm{f_z = \kappa Z^T z_0,} \tag{38}$$

If the displacement constrains for the overlap region can be described as:

$$\mathrm{z = u^o_{PD} - u^o_{FE} = u^o_{PD} - \sum_{\Omega_o} N(\xi) u^o_{FE},} \tag{39}$$

than the coupling matrix results in:

$$\mathrm{K_z} \begin{bmatrix} \mathrm{u^o_{PD}} \\ \mathrm{u^o_{FE}} \end{bmatrix} = \kappa \begin{bmatrix} \mathrm{I} & \mathrm{N_{PD}} \\ \mathrm{N^T_{PD}} & \mathrm{N^T_{PD} N_{PD}} \end{bmatrix} \begin{bmatrix} \mathrm{u^o_{PD}} \\ \mathrm{u^o_{FE}} \end{bmatrix}; \qquad \mathrm{f_z = 0,}$$

where I is a identity matrix, $\mathrm{N_{PD}}$ is a shape function applied on the peridynamic point to determine its position inside the finite element.

This all can be summarized to a system of coupled equations:

$$\begin{bmatrix} \alpha \mathbf{M}_{\mathrm{FE}} & \\ & (1-\alpha)\rho_{\mathrm{PD}} \end{bmatrix} \begin{bmatrix} \ddot{\mathbf{u}}_{\mathrm{FE}} \\ \ddot{\mathbf{u}}_{\mathrm{PD}} \end{bmatrix} + \begin{bmatrix} \alpha \mathbf{K}_{\mathrm{FE}} & \\ & (1-\alpha)\mathbf{f}_{\mathrm{PD}} \end{bmatrix} \begin{bmatrix} \mathbf{u}_{\mathrm{FE}} \\ \mathbf{u}_{\mathrm{PD}} \end{bmatrix} + \mathbf{K}_z \begin{bmatrix} \mathbf{u}^o_{\mathrm{PD}} \\ \mathbf{u}^o_{\mathrm{FE}} \end{bmatrix} = \begin{bmatrix} \alpha \mathbf{F}_{\mathrm{FE}} \\ (1-\alpha)\mathbf{b}_{\mathrm{PD}} \end{bmatrix} \tag{40}$$

It should be noted that the governing system of equations of FEM and PD differ in dimension by a certain factor. This problem can be overcome without loss of accuracy by multiplying the FE part by the volume of the finite element. In summary, the coupled problem to be solved looks as follows:

$$\begin{bmatrix} \frac{\alpha}{V_{\mathrm{el}}} \mathbf{M}_{\mathrm{FE}} & \\ & (1-\alpha)\rho_{\mathrm{PD}} \end{bmatrix} \begin{bmatrix} \ddot{\mathbf{u}}_{\mathrm{FE}} \\ \ddot{\mathbf{u}}_{\mathrm{PD}} \end{bmatrix} + \begin{bmatrix} \frac{\alpha}{V_{\mathrm{el}}} \mathbf{K}_{\mathrm{FE}} & \\ & (1-\alpha)\mathbf{f}_{\mathrm{PD}} \end{bmatrix} \begin{bmatrix} \mathbf{u}_{\mathrm{FE}} \\ \mathbf{u}_{\mathrm{PD}} \end{bmatrix} + \mathbf{K}_z \begin{bmatrix} \mathbf{u}^o_{\mathrm{PD}} \\ \mathbf{u}^o_{\mathrm{FE}} \end{bmatrix} = \begin{bmatrix} \frac{\alpha}{V_{\mathrm{el}}} \mathbf{F}_{\mathrm{FE}} \\ (1-\alpha)\mathbf{b}_{\mathrm{PD}} \end{bmatrix} \tag{41}$$

3.3 Splice Method

The method was first presented in 2016 by [25] as a practical coupling approach for static problems. The central concept is to divide the entire domain into two parts: one discretized with finite elements (FE) and the other with peridynamic (PD) points, ensuring that they do not overlap (Fig. 5).

The main idea of the coupling method is that PD points, that located near the coupling boundary, can "see" the FE nodes through a defined horizon δ. The PD points, that are

close to the coupling interface have not only other PD points in their non-local neighborhood, but also FE nodes inside. Consequently, they have non-local interactions with all of them, thereby completing the non-local neighborhood of the PD points.

In the finite element framework, nodes interact only with their direct neighbors and this continues until the last element, that would consists of both FE nodes and PD points. Let these elements be called coupled elements. The coupled elements exhibit the properties of both fields, which is also reflected in the construction of the stiffness matrix.

In the above-mentioned paper, the linearized version of peridynamics is employed, which allows the decoupling of stiffness and displacement components from internal bond force density in Equation (17). By the assumption of small deformation: $|\boldsymbol{\eta}| \ll 1$, the second-order micromodulus tensor $\mathbb{C}$ is given by: $\mathbb{C} = \frac{\partial \mathrm{f}}{\partial \boldsymbol{\eta}}(0, \boldsymbol{\xi})$ [8]. This formulation enables to assemble the stiffness matrix for peridynamics. To couple two domains, it is necessary to create a global FEM-PD stiffness matrix by assembling and combining the individual matrices corresponding to their respective global points.

It can be noticed that the global stiffness matrix is non-symmetric since the number of non-diagonal terms for PD nodes exceeds that for FEM nodes. This approach can also be applied to dynamic analysis to assemble a global mass matrix. The further works by [59] and [60] provide more detailed information regarding the coupling procedure.

4 Numerical results

The comprehensive review of different FEM–PD coupling methods with verification on static cases has already been presented in [61]. Many of these methods demonstrate promising results and show good agreement with the reference solutions. However, static analyses alone do not provide sufficient information on the quality of the coupling schemes, since the main field of application for coupled FEM–PD approaches lies in dynamic fracture.

When a crack initiates and propagates under load, high–frequency waves are generated as a result of the fracture process. Therefore, this study focuses particularly on the dynamic behaviour of coupled systems. As demonstrated in Sect. 2.3, elastic waves in classical elasticity and in peridynamics show different characteristics. Unlike in the classical case, peridynamic waves display dispersive behavior. It is proposed that the wave parameters and numerical values be selected so that in the PD case (Fig. 1), the value $\frac{k\delta}{2\pi}$ approaches zero, thereby approximating the classical case.

To validate the coupling methods, we consider two benchmark tests (Fig. 6) and compare the results against both numerical FE and PD reference solutions.

Free vibration test: Consider an elastic one-dimensional bar with a constant cross-section area $A = 4 \cdot 10^{-8}$ m^2 and a length $L = 1$ m that is fixed at $\mathrm{x} = 0$ and initially pre-strained so that the bar has a homogeneous deformation: at $t = 0$, $\mathrm{u}(\mathrm{x}, t_0) = \frac{\mathrm{x}}{L}\mathrm{u}_0$ (Fig. 6a). The bar is released at time $t > 0$, and free vibrations occur. The material constants of the bar are $E = 10^9$ Pa, $\nu = 0.25$ and $\rho = 7800$ kg/m^3. For the reference FE solution the bar discretizes with the element size $\Delta \mathrm{x}_{\mathrm{FE}} = 1 \cdot 10^{-3}$ m, while the PD numerical parameters are: $\Delta \mathrm{x}_{\mathrm{PD}} = 2 \cdot 10^{-4}$ m and horizon $\delta = 3.015\, \Delta \mathrm{x}_{\mathrm{PD}} = 6.03 \cdot 10^{-4}$ m. The time domain parameters are chosen as $\Delta t = 1.5 \cdot 10^{-7}$ s and $t_{\mathrm{end}} = 1.3 \cdot 10^{-3}$ s.

Since the PD equation of motion does not contain a spatial derivative of displacement, no natural boundary conditions arise when deriving the equilibrium equation. So the choice of PD boundary conditions needs to be clarified. For the fixed left side of the bar, the additional fictitious domain with size of $3\Delta \mathrm{x}_{\mathrm{PD}}$ is modeled, where the displacement $\mathrm{u} = 0$ is applied. To all the real points where $\mathrm{x} \neq 0$ and $t = 0$ the prescribed displacement $\mathrm{u}(\mathrm{x}, t_0)$ is applied. Also, the volume correction strategy from [7] is used to improve the inaccuracies in PD numerical integration.

Figure 7 displays the displacement over the time of the last point of the bar at $\mathrm{x} = L$ for both FE and PD solutions. The plot is enlarged around the time $t = 0.005$ s and $t = 0.011$ s. As expected, the difference between the solutions is negligibly small, since the PD solution converges to classical elasticity by $\delta \to 0$ [62].

Wave propagation test: Consider an elastic one-dimensional bar with a constant cross-section area $A = 1 \cdot 10^{-6}$ m^2 and a length $L = 5$ m (Fig. 6b). It is fixed at $\mathrm{x} = 0$ and

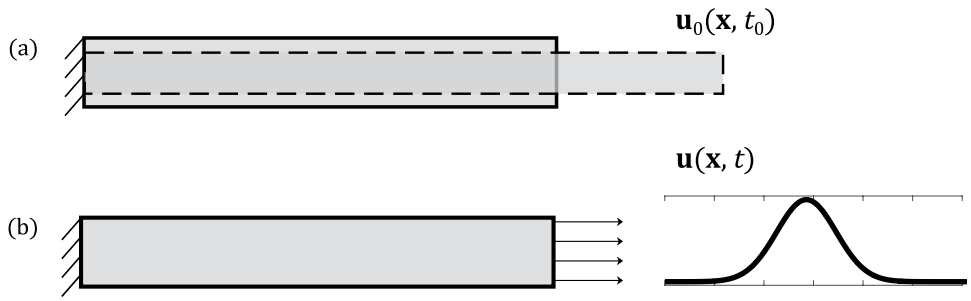

Fig. 6 Two benchmark tests to validate the coupling methods

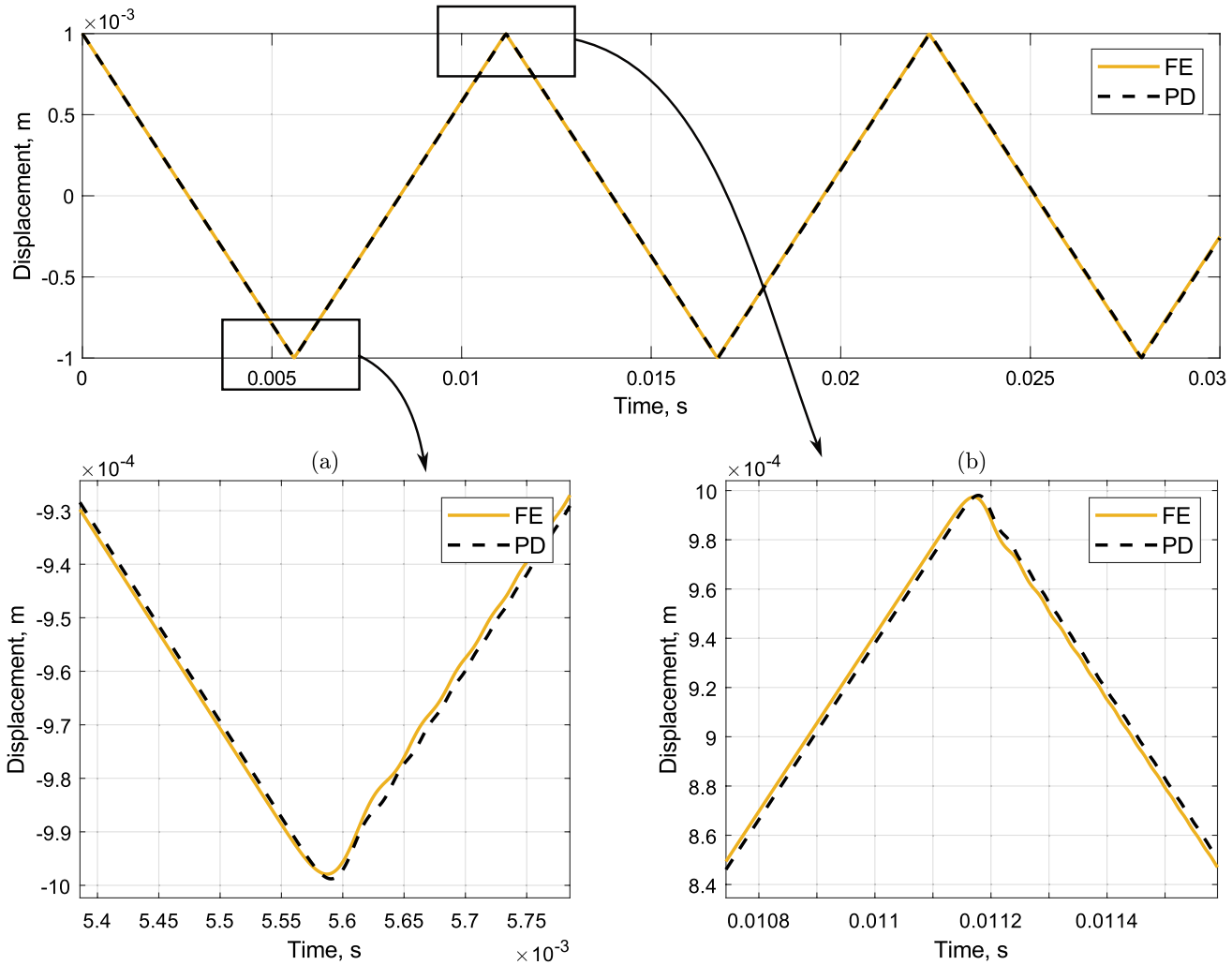

Fig. 7 Comparison of FE and PD solutions in a free vibration test. The enlarged displacement in point $x = L$ around the time **a** $t = 0.005$ s and **b** $t = 0.011$ s

exited with a prescribed displacement at $x = L$. As a prescribed displacement wave the sine type wave is chosen: $u(L,t) = A_1 \sin(f_r t - \pi/2) + c$ with the following parameters: $A_1 = 0,5\,10^{-4}$ m, $c_1 = 0.5\,10^{-4}$ m, $f_r = 79,5$ Hz. The material constants of the bar are $E = 10^9$ Pa, $\nu = 0.25$ and $\rho = 7800\ \mathrm{kg/m^3}$.

For PD boundary conditions on the left side of the bar, an additional fictitious region of a size $3\Delta x_{PD}$ is modeled, where the displacement is set to zero $u = 0$. The displacement wave is applied over the time on the last real node at $x = L$. To improve the numerical integration, the volume correction schema is used as in a previous test. For the reference FE and PD solutions, the following numerical parameters are chosen: $\Delta x_{FE} = 3.3 \cdot 10^{-3}$ m, $\Delta x_{PD} = 1 \cdot 10^{-3}$ m, $\delta = 3.015\,\Delta x_{PD}$, $\Delta t = 2.7 \cdot 10^{-7}$ s, $t_{end} = 1.4 \cdot 10^{-3}$ s.

Figure 8 shows the wave at $t = 6.8 \cdot 10^{-5}$ s and $t = 1.2 \cdot 10^{-3}$ s. The wave moves from the right side of the bar to the left. The plot is enlarged to analyze the difference between the solutions. As expected, the disagreement is negligibly small, and the PD converges to the FE solution with current numerical variables. Therefore, for analyzing the coupling strategies, only the PD solution is used as a reference.

4.1 Arlequin coupling case

4.1.1 Free vibration test

Very often, the effectiveness of numerical methods depends on choosing the right parameters. Figure 9 shows the displacement of the last point of the bar over time, calculated with Arlequin method in comparison with the pure PD case (upper plot). Figure 9a-c displays the parameter study for Arlequin coupling at close near $t = 5.6 \cdot 10^{-3}$ s. The mesh density study is conducted to evaluate the convergence rate

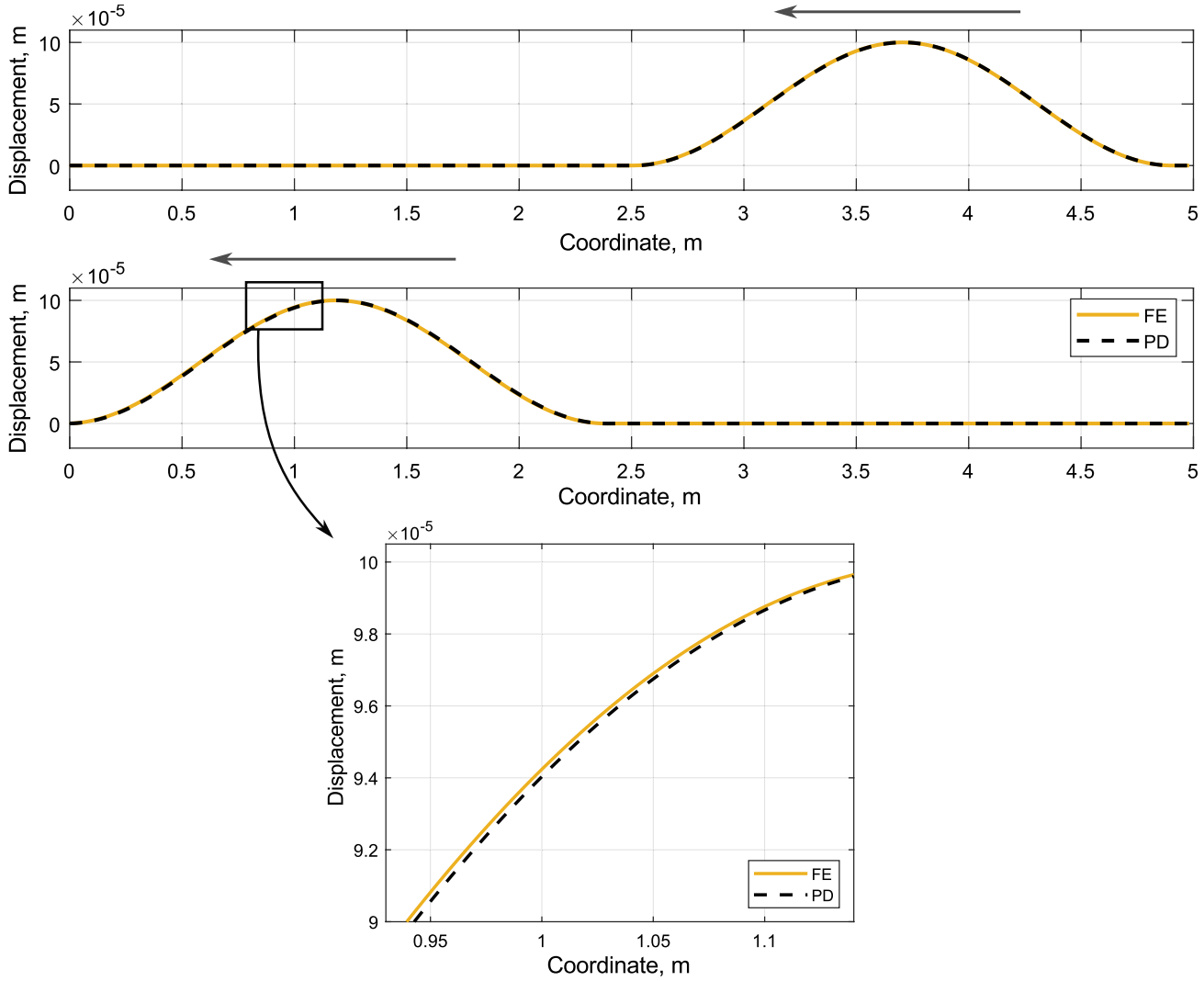

Fig. 8 Comparison of FE and PD solutions in a wave propagation test. Displacement of a bar at $t = 6.8 \cdot 10^{-5}$ s and $t = 1.2 \cdot 10^{-3}$ s for a sine-type wave

and to compare the performance with other coupling methods. From this study, it can be observed that the highest accuracy with respect to the reference solution is achieved when the grid spacing is reduced to $\Delta \mathrm{x} = 2 \cdot 10^{-4}$ m.

The influence of penalty parameters is illustrated in plot (b). If it is chosen too small, numerical errors may occur in the solution [40]. However, revealing a general rule for selecting an appropriate parameter remains a challenging problem. The coupling properties theoretically improve as the parameter κ increases. However, its value is numerically limited [33]. Choosing κ too large can result in numerical instability as the determinant of the stiffness matrix approaches zero. Based on the analysis of three cases, it's evident that improving κ to the value 10^6 leads to a good agreement with the PD case.

Furthermore, the size of the overlapping area is investigated in Fig. 9c with one element in the overlap zone, three elements corresponding to the approximate value of the horizon, and six elements as the value of two horizons. All three solutions yield similar results, so the parameter study should be continued by another test configuration.

4.1.2 Wave propagation test

Figure 10 shows the displacement at $t = 6.8 \cdot 10^{-5}$ s and $t = 1.2 \cdot 10^{-3}$ s, which corresponds to the time before and after passing the coupled region. The black vertical line matches the transition from the FE part (left) to the PD (right). To analyze the convergence to the reference solution, the plots of the displacement around the main wave and the remaining part at $t = 1.2 \cdot 10^{-3}$ s are enlarged. The plot in Fig. 10a corresponds to the enlarged displacement of a bar. A coarse mesh causes a lag in wave propagation, as detailed in graph (b). Here, the left part of the bar is enlarged, and

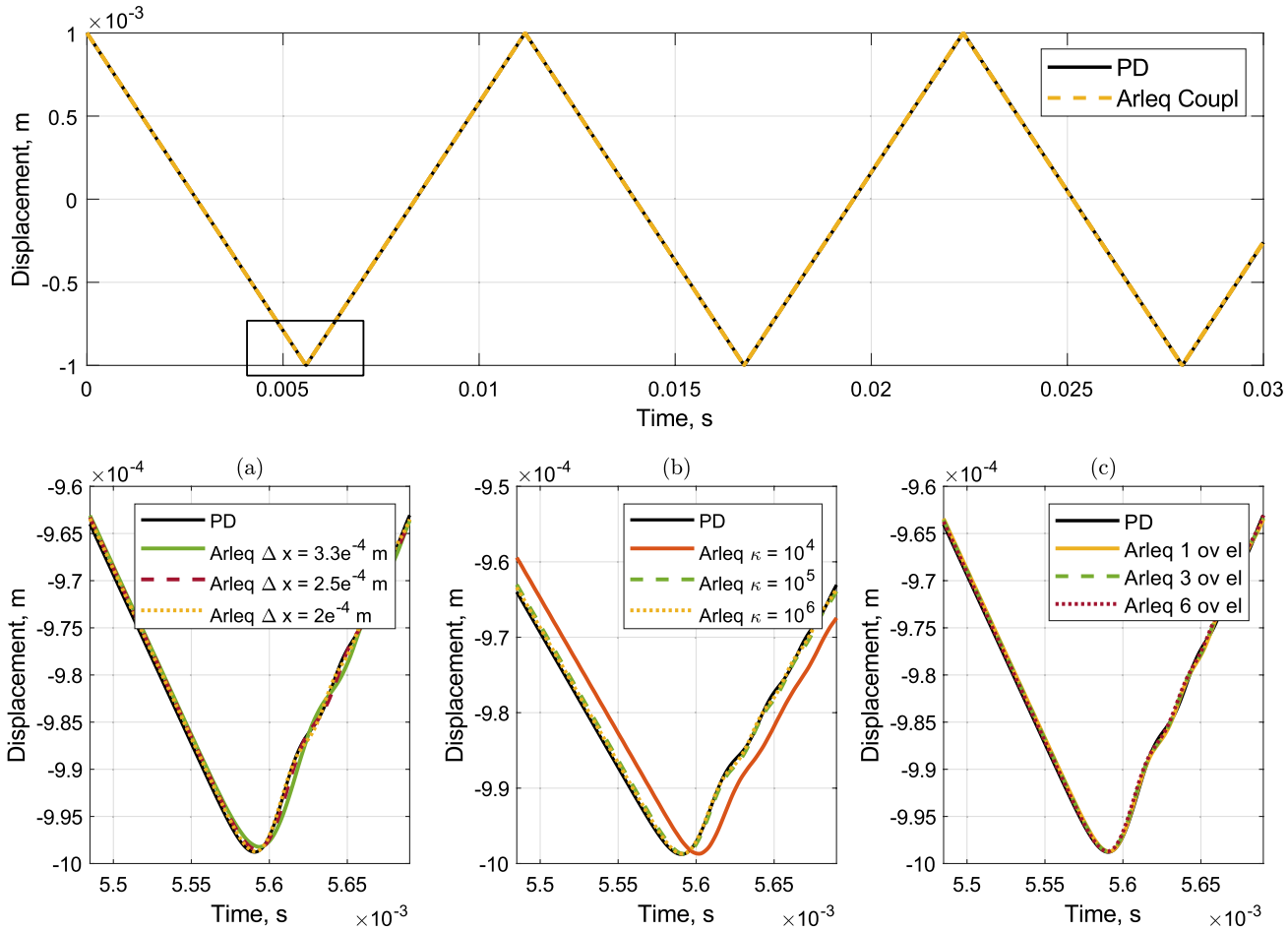

Fig. 9 A case study in a free vibration test for Arlequin coupling case vs reference peridynamic solution for displacement in the point $x = L$ over time: **a** mesh density study; **b** penalty number study; **c** size of overlapping area study

one can note that by passing a coupled interface, the part of the main wave reflects and travels in the opposite direction. The reflected wave has the same speed and frequency as the main one. By reducing the grid size, the reflection decreases to the amplitude value of $\approx 3.9 \cdot 10^{-9}$ m. One can mention, that the amplitude of the reflected wave is insignificant small in comparison to the main wave amplitude ($\approx 0.004\%$). Analyzing the size of the overlapping region (Fig. 11a), it can be seen that an increase of the overlapping zone leads to a disturbance between local and non-local parts of the bar, resulting in an increase in the amplitude of the reflected wave. Additionally, three κ values have been considered (Fig. 11b). In conclusion, the careful choice of numerical parameters made the reflected wave minimal, so it is not visible and practically can be neglected.

4.2 Schwarz coupling case

4.2.1 Free vibration test

The Schwarz coupling method, a well-established technique, may need some adjustments when coupled with a non-local domain. Specifically, the selection of boundary interfaces Γ_1 and Γ_2 (Fig. 2) deserve special attention. This is because the material point in the PD interacts with other points through a horizon, potentially transforming the interfaces into boundary domains that are several layers thick.

Let us consider five possible configurations to calibrate the Schwarz procedure:

- Case 1: Interfaces Γ_1 and Γ_2 are one element thick: $\Gamma_1 = \Gamma_2 = \Delta x$;
- Case 2: Interfaces Γ_1 is one element thick, while Γ_2 has thickness of horizon: $\Gamma_1 = \Delta x, \Gamma_2 = \delta$;

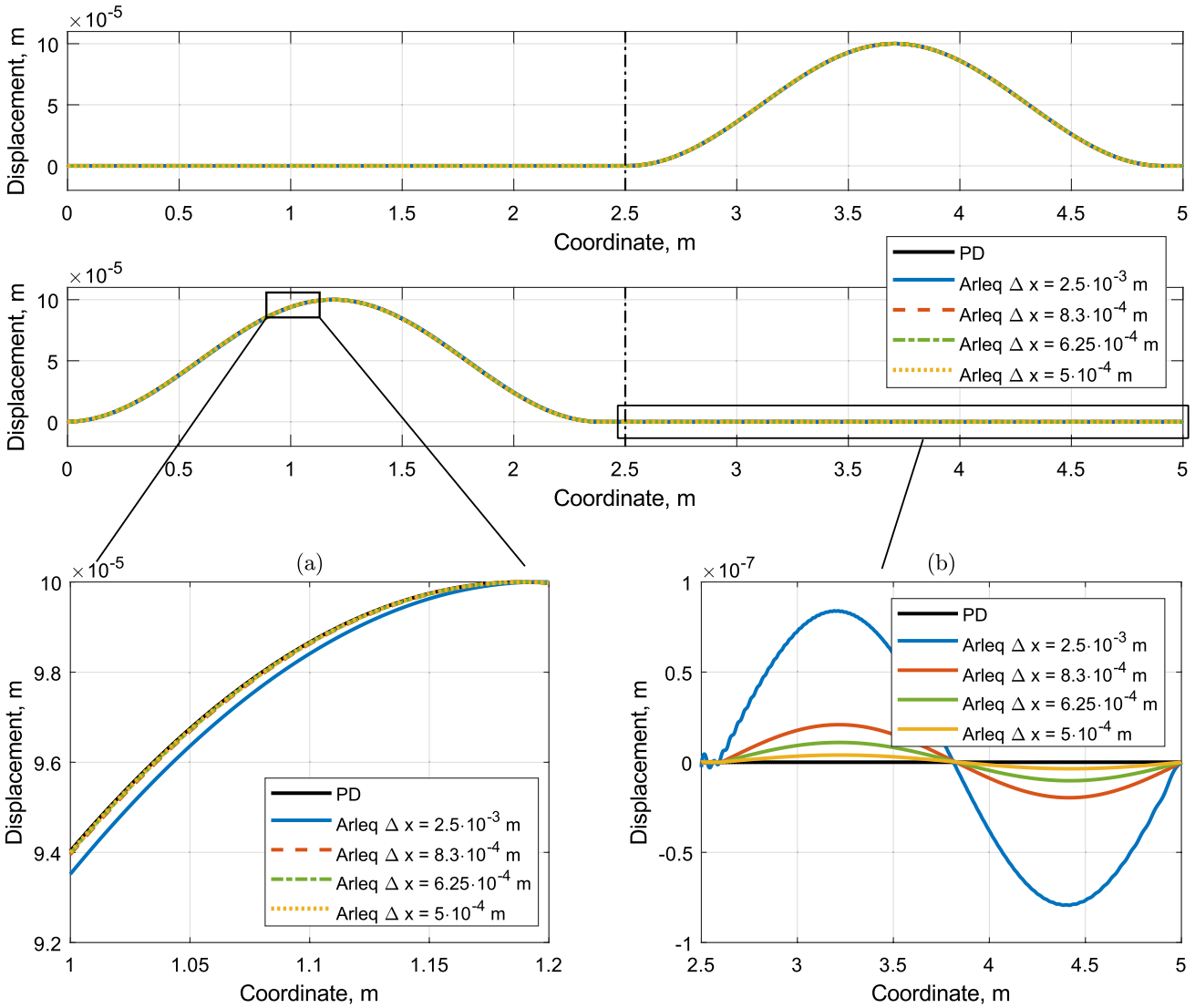

Fig. 10 Displacement of a bar at $t = 6.8 \cdot 10^{-5}$ s and $1.2 \cdot 10^{-3}$ s for a sine-type wave propagation test for Arlequin coupling case vs reference peridynamic solution: **a** mesh density study; **b** mesh density study regarding reflected wave amplitude

- Case 3: Γ_1 has thickness of horizon, while interface Γ_2 is one layer thick:
  $\Gamma_1 = \delta, \Gamma_2 = \Delta$x;
- Case 4: Both domains have thickness of horizon:
  $\Gamma_1 = \Gamma_2 = \delta$;
- Case 5: Both domains have thickness of two horizons:
  $\Gamma_1 = \Gamma_2 = 2\delta$.

Consider a 1D bar with the geometry and material parameters from the Sect. 4.1.1. The grid spacing for both PD and FEM domains are the same: Δx $= 1.43 \cdot 10^{-4}$ m. The critical time step is $\Delta t = 2.5 \cdot 10^{-7}$ s.

Figure 12 (upper plot) shows displacement of the last point of the bar over time for all five Schwarz cases with a comparison of the pure PD solution. It's clear that both Case 1 and Case 2 give a non-physical response, indicating that the solution is insensitive to the choice of Γ_2 thickness, which is not the case for boundary domain Γ_1. It is to consider further analyzing case 3,4,5 in the present test configuration.

For the detailed analyses of the remaining cases, the displacement is enlarged, as it is shown on the upper plot. It is important to notice, that the solutions of the remaining Schwarz cases fluctuate around the reference PD solution - plots (a) and (b). The closest the PD solution has the Case 5. Since the Cases 1 and 2 give the nonphysical results, just the remaining Schwarz Cases are considered further.

4.2.2 Wave propagation test

Figure 13 shows the wave before and after passing the coupling region, the wave moves from the right side of the bar

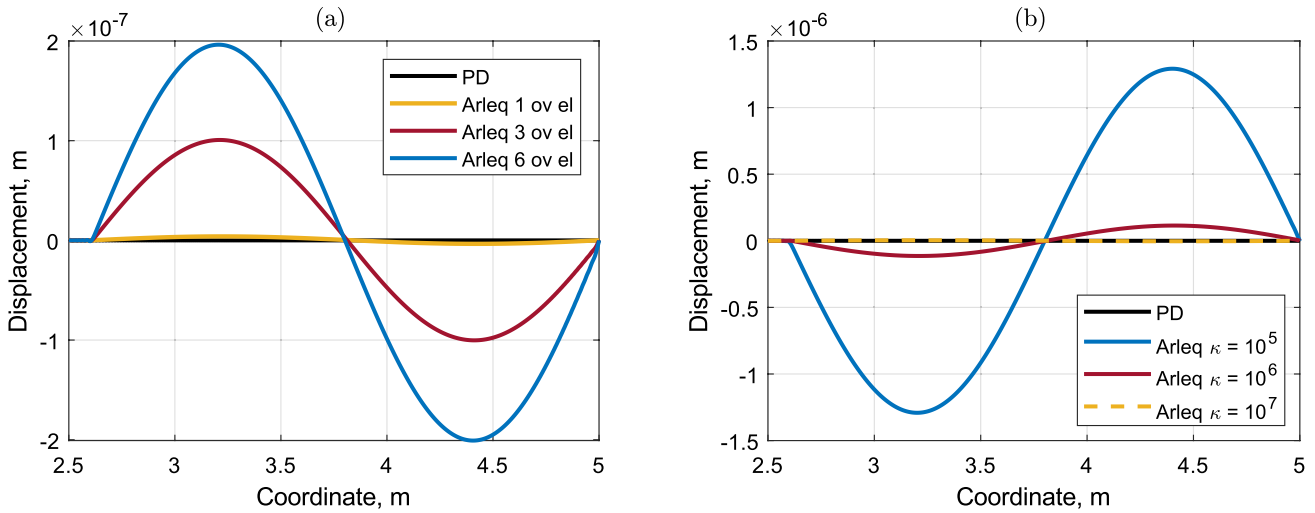

Fig. 11 Parameter study for the bar at $t = 1.2 \cdot 10^{-3}$ s for sine-type wave propagation for Arlequin coupling solution vs reference peridynamic solution: **a** size of overlapping area study; **b** κ - value study

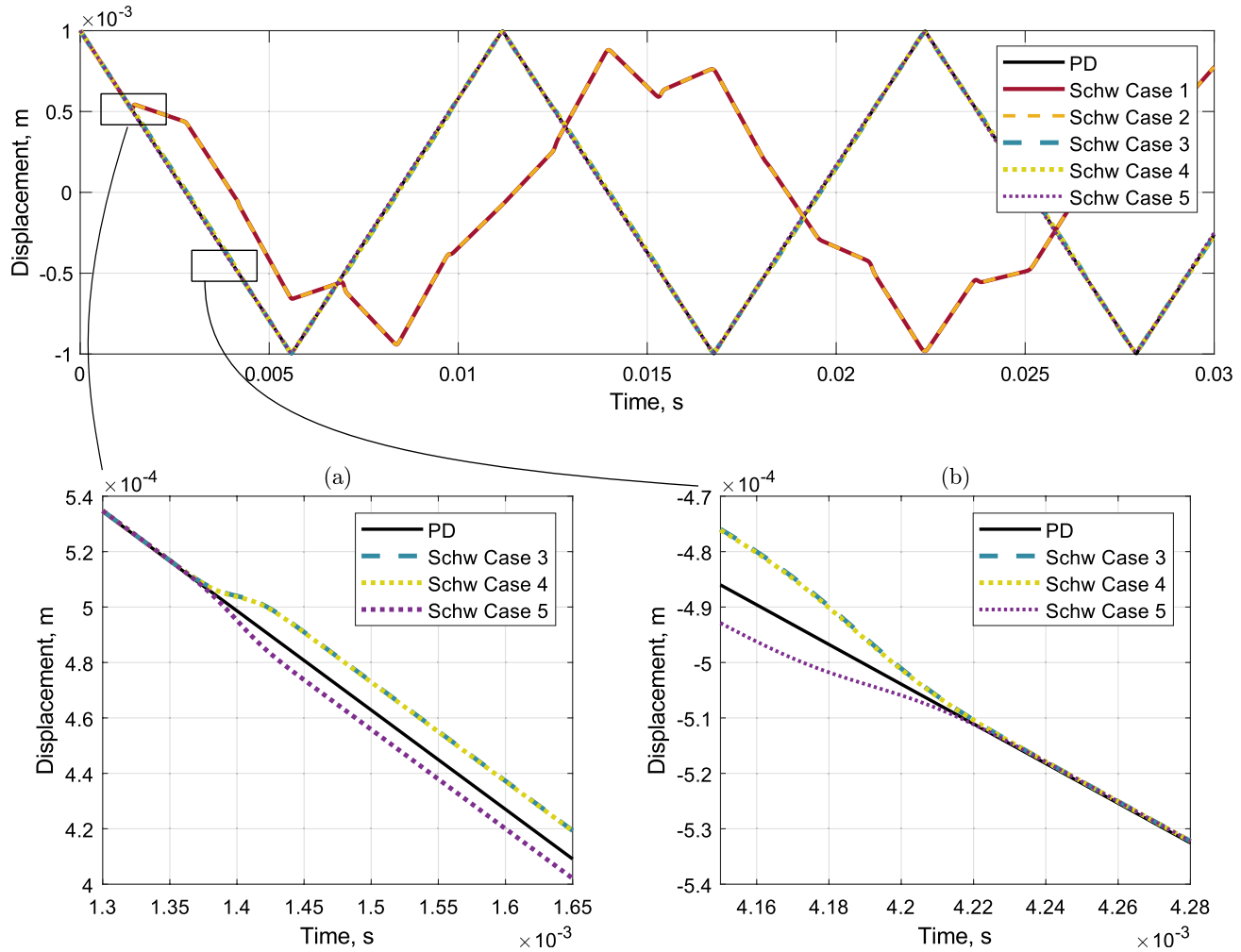

Fig. 12 A case study in a free vibration test for Schwarz coupling case vs reference peridynamic solution for displacement in the point x $= L$ over time: **a** enlarged displacement around an upper chosen rectangle for Cases 3,4,5; **b** enlarged displacement around a bottom chosen rectangle for Cases 3,4,5

to the left. The time step is chosen as $\Delta t = 1.6 \cdot 10^{-7}$ s. One can mention that there is no visible reflection from the coupling zone, so the displacement on the right side of the bar at time $t = 1.2 \cdot 10^{-3}$ s needs to be enlarged.

Figure 13a displays the grid density study for the Schwarz Case 3 to investigate the convergence speed. With the grid spacing $\Delta x = 5 \cdot 10^{-3}$ m, parasite vibrations appear. However, when the grid distance is $\Delta x = 7.1 \cdot 10^{-4}$ m the displacement line appears smooth without additional numerical perturbations. The amplitude of the reflected wave remains constant, independent of mesh density, which is not the case in the Arlequin method. Nevertheless, the reflected amplitude value $\approxeq 4 \cdot 10^{-9}$ m ($0,004\%$ of the main amplitude) is relatively small and produces a comparable result with the previous method.

Figure 13b presents the reflected wave for Cases 3,4 and 5 and it can be mentioned that there is no noticeable difference is detected between all of them. The explanation could be as follows: both interfaces are used for transmitting information between two independent domains. When the local domain transmits information, it only needs for information to be "local", whereas the non-local domain should transmit ”non-local” information, meaning that a boundary region should have a thickness at least equal to the horizon.

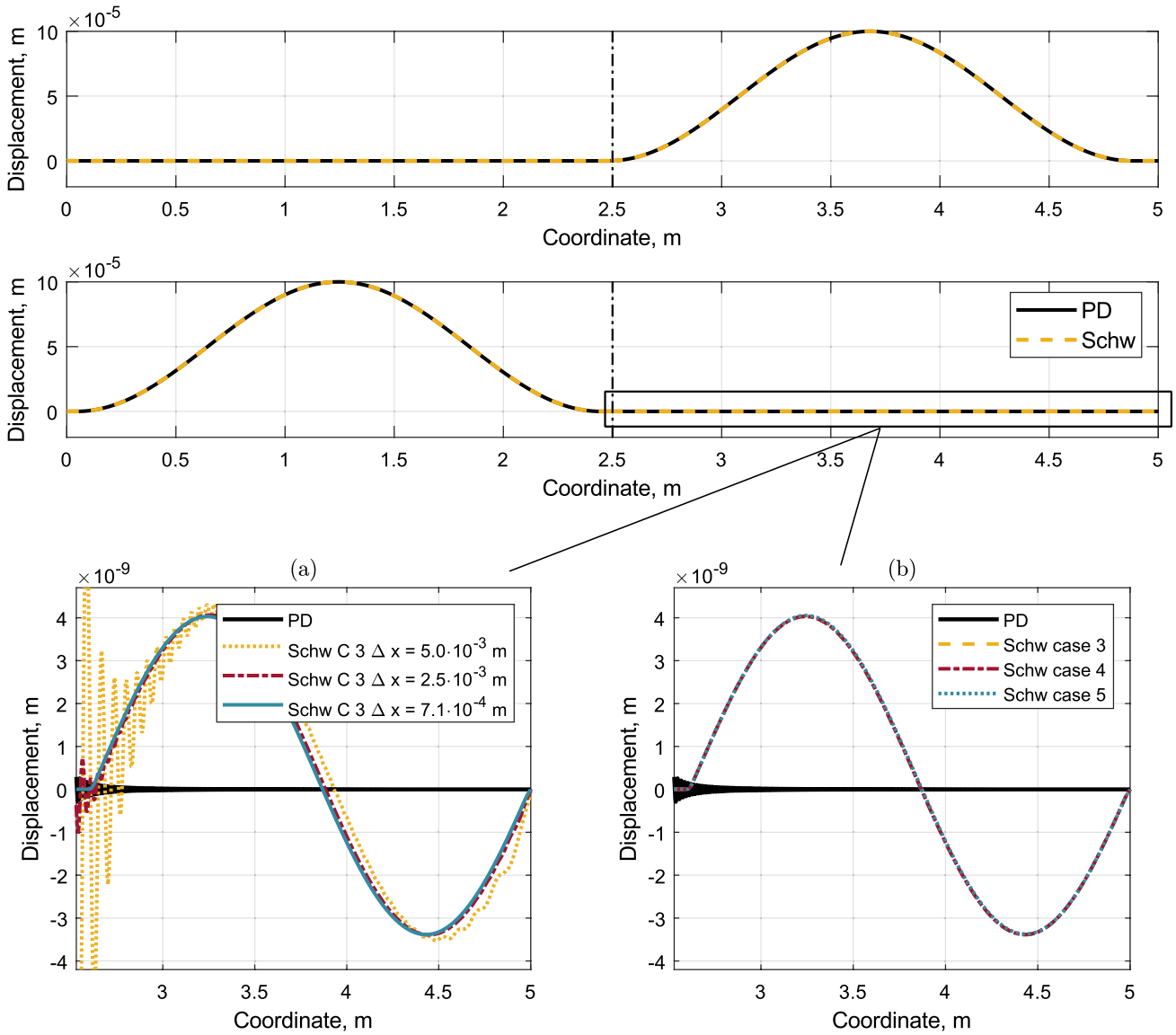

Fig. 13 A case study of a sine-type wave propagation test for different Schwarz configurations vs reference peridynamic solution at $t = 6.8 \cdot 10^{-5}$ s and $t = 1.2 \cdot 10^{-3}$ s: **a** mesh density study for Schwarz Case 3 around the reflected wave; **b** displacement of the right part of a bar around the reflected wave

4.3 Splice coupling case

4.3.1 Free vibration test

Figure 14 shows the solution of the Splice coupled method in comparison to the PD. Unlike to other methods, the Splice method doesn't have any additional numerical parameters to investigate, except mesh density. Thus the displacement around $t = 5.6 \cdot 10^{-3}$ s and $t = 2.2 \cdot 10^{-2}$ s is enlarged for close consideration. It is to mention, that the solution oscillates around the reference PD case and the decrease of mesh density from $\Delta x = 5 \cdot 10^{-4}$ m to $\Delta x = 2.5 \cdot 10^{-4}$ m doesn't bring any significant difference in the amplitude of this oscillations.

4.3.2 Wave propagation test

As before, the test configuration was taken from the Sect. 4.1.2. One can mention no reflected wave on the right part of a bar on the Fig. 15. The enlarged displacements on the left (plot (a)) and on the right part of the bar (plot (b)) show slightly difference by reducing the mesh density to $\Delta x = 5 \cdot 10^{-4}$ m. Again the solution oscillates around the reference PD case, but decreasing the grid size leads to minimization of the amplitude of oscillation as well as slightly reduction of reflected wave amplitude. The amplitude of the reflected wave results in $\approxeq 0.65 \cdot 10^{-9}$ m, that corresponds to 0.00065% of the main wave amplitude.

5 Conclusions

The study explored the effectiveness of the Arlequin, Schwarz and Splice coupling methods in simulating the dynamic response of a one-dimensional bar subjected to free vibration and wave propagation tests. The results lead to several conclusions.

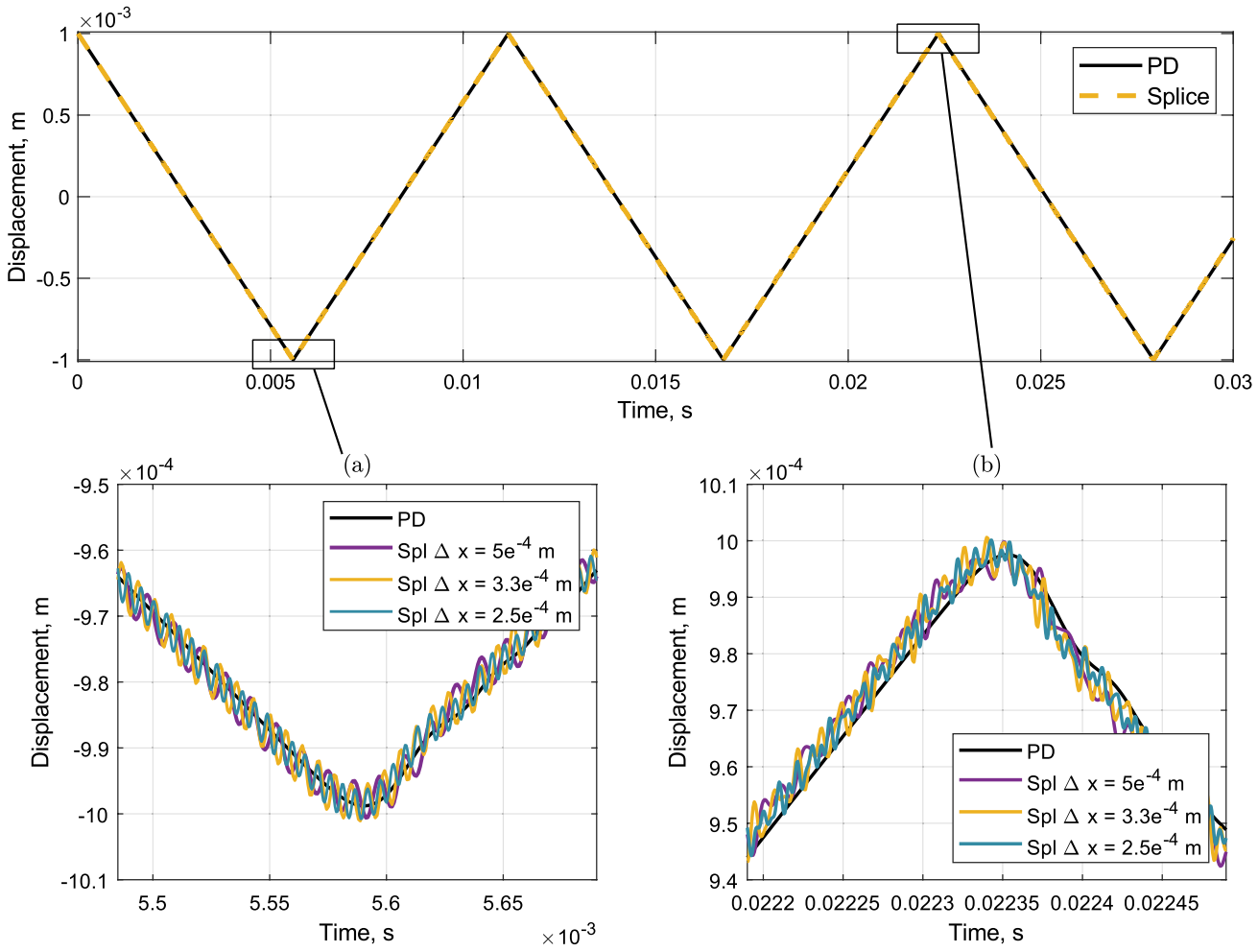

Fig. 14 A case study in a free vibration test for Splice coupling case vs reference peridynamic solution for displacement in the point $x = L$ over time: **a** enlarged displacement around left chosen rectangle for mesh density study; **b** enlarged displacement around right chosen rectangle for mesh density study

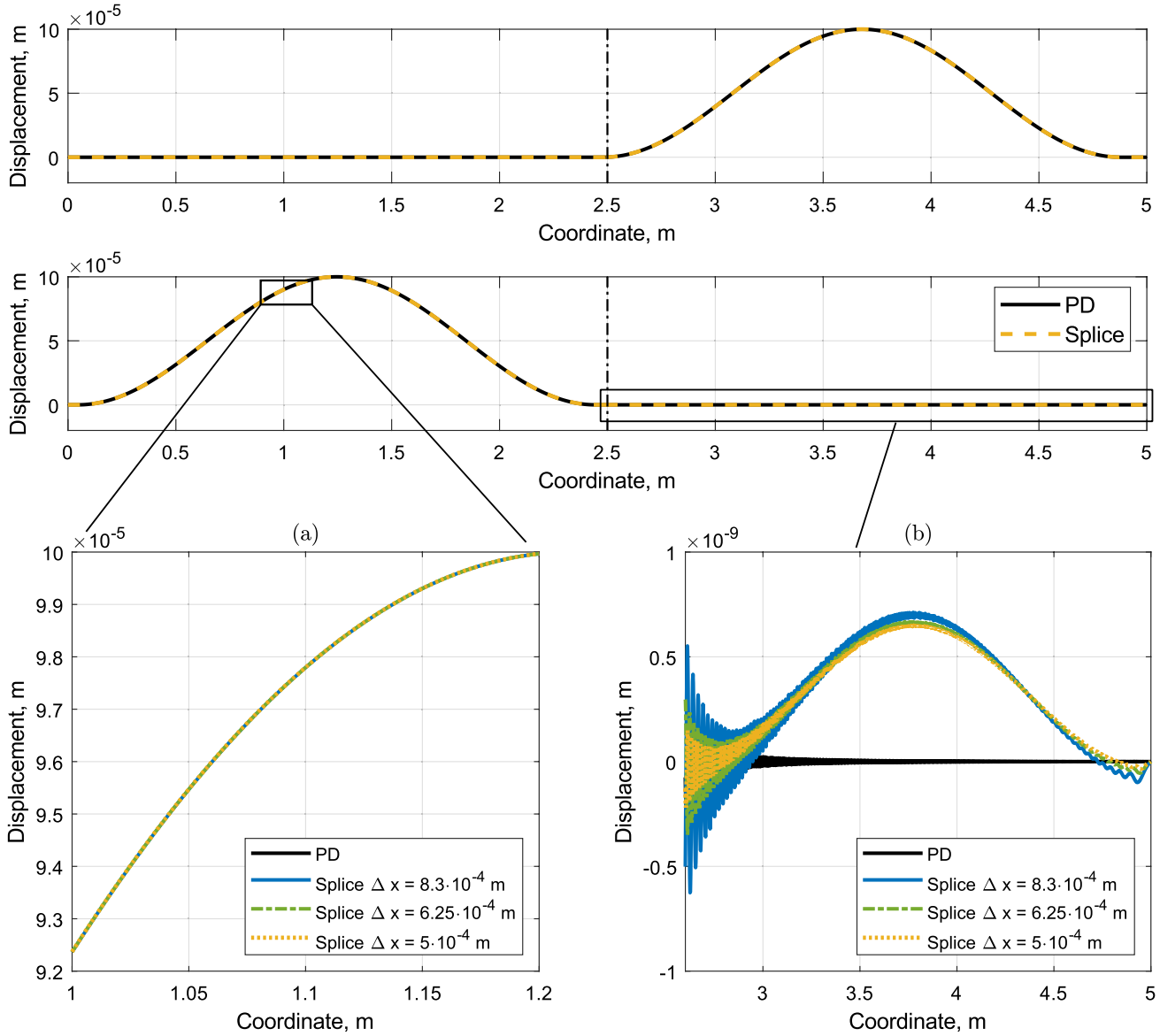

Fig. 15 A case study of a sine-type wave propagation test for Splice coupling method vs reference peridynamic solution: **a** enlarged displacement for mesh density study; **b** enlarged displacement around the reflected wave for mesh density study

The Arlequin Method demonstrated high accuracy when the mesh density and penalty parameters were appropriately selected. The displacement results closely matched the reference peridynamic (PD) solutions when a fine mesh density ($\Delta x = 2 \cdot 10^{-4}$ m for free vibration test) and an optimized penalty parameter ($\kappa = 10^6$) were used. It was observed that an incorrect selection of these parameters could lead to significant numerical errors and interpenetration issues. The method showed good convergence to the reference solution in the wave propagation test as well. The optimal configuration effectively minimized the amplitude of the reflected wave, confirming the method's robustness in handling dynamic crack propagation simulations.

Considering the Schwarz Method, it requires careful selection of boundary interfaces to ensure accurate results. Case 5 ($\Gamma_1 = \Gamma_2 = 2\delta$) provided the closest match to the PD solution, while cases with thinner boundary interfaces resulted into larger errors or non-physical responses. This indicates that the method's effectiveness is highly sensitive to the chosen boundary configuration. Similar to the Arlequin method, the Schwarz Method achieved satisfactory results in the sine-type wave propagation test. Cases 3,4 and 5 provided the reliable results, with minimal amplitude of reflected waves, comparable to the Arlequin Method. The mesh density had a noticeable impact on the presence of numerical perturbations, with finer meshes producing smoother displacement profiles.

The Splice Method is intuitive clear and easy for numerical implementation. It has an advantage, that there is no numerical parameters to calibrate. The method showed a good convergence to the reference PD solution for both free vibration and wave propagation tests. Nevertheless, a numerical effect has been notices, that the coupled solution oscillates around the reference one. The decrease of grid size has an influence on the amplitude of this oscillations, but they cannot be completely eliminated.

The mesh density study was conducted to determine which method converges faster to the reference solution. It can be observed that the Schwarz method exhibits faster convergence in the wave propagation test, whereas the Splice method performs better in the vibration analysis.

Overall, all of the coupling methods demonstrated strong potential for accurate dynamic simulations, provided that specific parameter configurations were used. The Arlequin method proved effective with a well-chosen penalty parameter and mesh density, while the Schwarz method showed sensitivity to boundary interface selection. The Splice Method is independent from numerical parameters, but the solution exhibited slight fluctuations, that could possibly have an effect in 2D or 3D analysis.

The pure PD model exhibites inherent dispersive characteristics. These characteristics influenced the accuracy and stability of the coupled simulations. While all the coupling methods managed to achieve satisfactory results, there were discrepancies when compared to the finite element method (FEM) solutions. These discrepancies highlight the challenges in perfectly matching the non-local PD model with the local FEM model.

Further investigation into the dispersive properties of PD and their impact on coupled simulations would help in achieving a more seamless integration with FEM, ensuring improved accuracy, stability and applicability of these methods in complex dynamic scenarios.

Acknowledgements The project is funded by the Deutsche Forschungsgemeinschaft (DFG, German Research Foundation) under the Project GA480/16-1 (No 456427423). This financial support is gratefully acknowledged.

Funding Open Access funding enabled and organized by Projekt DEAL.

References

1. Cherepanov GP (1974) Mechanics of brittle fracture (Mekhanika khrupkogo razrusheniya). Nauka, Moskow
2. Belytschko T, Moes N, Doldow J (1999) A finite element method for crack growth without remeshing. Int J Numer Meth Eng 46(1):131–150
3. Scheider I, Cornes A, Schwalbe K-H (2009) The siam method for applying cohesive models to the damage behaviour of engineering materials and structures. GKSS-Forschungszentrum Geesthacht GmbH (Germany)
4. Borden MJ, Verhoosel CV, Scott MA, Hughes TJR, Landis CM (2012) A phase-field description of dynamic brittle fracture. Comput Methods Appl Mech Eng 217:77–95
5. Zhou SJ, Lomdahl PS, Thomson R, Holian BL (1996) Dynamic crack processes via molecular dynamics. Phys Rev Lett 76(13):2318–2321
6. Abraham F, Brodbeck D, Rudge W (1996) A molecular dynamics investigation of rapid fracture mechanics. J Mech Phys Solids 9:1595–1619
7. Bobaru F, Foster JT, Geubelle PH, Silling SA (2015) Handbook of peridynamic modeling. Modern mechanics and mathematics. Taylor and Francis, NY
8. Silling SA (2000) Reformulation of elasticity theory for discontinuities and long-range forces. J Mech Phys Solids 48:175–209
9. Silling SA, Epton M, Weckner O, Xu J, Askari E (2007) Peridynamic states and constitutive modeling. J Elast 88(2):151–184
10. Weckner O, Askari A, Xu J, Razi H, Silling S (2007) Damage and failure analysis based on peridynamics - theory and applications. In: 48th AIAA/ASME/ASCE/AHS/ASC structures, structural dynamics, and materials conference, Reston, Virigina, 04232007. American Institute of Aeronautics and Astronautics
11. Yolum U, Gök E, Coker D, Guler MA (2018) Peridynamic modelling of delamination in dcb specimen. Procedia Struct Integrity 13:2126–2131
12. Mitts C, Naboulsi S, Przybyla C, Madenci E (2020) Axisymmetric peridynamic analysis of crack deflection in a single strand ceramic matrix composite. Eng Fract Mech 235:107074
13. Rädel M, Willberg C, Krause D (2019) Peridynamic analysis of fibre-matrix debond and matrix failure mechanisms in composites under transverse tensile load by an energy-based damage criterion. Compos B Eng 158:18–27
14. Silling SA, Askari A (2004) Peridynamic modeling of impact damage. Problems involving thermal hydraulics, liquid sloshing, and extreme loads on structures, pages 197–205
15. Ren B, Song J (2022) Peridynamic simulation of particles impact and interfacial bonding in cold spray process. J Therm Spray Technol 31(6):1827–1843
16. Oterkus E, Guven I, Madenci E (2012) Impact damage assessment by using peridynamic theory. Open Eng 2(4):523–531
17. Hesse J-T, Willberg C, Hein R, Winkelmann F (2023) Peridynamic framework to model additive manufacturing processes. PAMM 23(4):e202300033
18. Javili A, Morasata R, Oterkus E, Oterkus S (2019) Peridynamics review. Math Mech Solids 24(11):3714–3739
19. Zhanping X, Zhang G, Chen Z, Bobaru F (2018) Elastic vortices and thermally-driven cracks in brittle materials with peridynamics. Int J Fract 209(1–2):203–222
20. Wang B, Oterkus S, Oterkus E (2021) Thermal diffusion analysis by using dual horizon peridynamics. J Therm Stresses 44(1):51–74

21. Agwai A, Guven I, Madenci E (2011) Crack propagation in multilayer thin-film structures of electronic packages using the peridynamic theory. Microelectron Reliab 51(12):2298–2305
22. Qi J, Li C, Tie Y, Zheng Y, Cui Z, Duan Y (2024) A peridynamic-based homogenization method to compute effective properties of periodic microstructure. Computat Particle Mech 11(3):1391–1401
23. Diana V, Bacigalupo A, Lepidi M, Gambarotta L (2022) Anisotropic peridynamics for homogenized microstructured materials. Comput Methods Appl Mech Eng 392:114704
24. Cavuoto R, Deseri L, Fraldi M (2024) Effects of a nonlocal microstructure on peeling of thin films. Meccanica 59(8):1269–1283
25. Galvanetto U, Mudric T, Shojaei A, Zaccariotto M (2016) An effective way to couple fem meshes and peridynamics grids for the solution of static equilibrium problems. Mech Res Commun 76:41–47
26. Mossaiby F, Sheikhbahaei P, Shojaei A (2022) Multi-adaptive coupling of finite element meshes with peridynamic grids: robust implementation and potential applications. Eng Comput 39:2807–2828
27. Liu W, Hong J-W (2012) A coupling approach of discretized peridynamics with finite element method. Comput Methods Appl Mech Eng 245–246:163–175
28. Yue Yu, Bargos FF, You H, Parks ML, Bittencourt ML, Karniadakis GE (2018) A partitioned coupling framework for peridynamics and classical theory: analysis and simulations. Comput Methods Appl Mech Eng 340:905–931
29. Seleson P, Beneddine S, Prudhomme S (2013) A force-based coupling scheme for peridynamics and classical elasticity. Comput Mater Sci 66:34–49
30. Lubineau G, Azdoud Y, Han F, Rey C, Askari A (2012) A morphing strategy to couple non-local to local continuum mechanics. J Mech Phys Solids 60(6):1088–1102
31. Serge Prudhomme H, Ben Dhia PT, Bauman NE, Oden JT (2008) Computational analysis of modeling error for the coupling of particle and continuum models by the Arlequin method. Comput Methods Appl Mech Eng 197(41–42):3399–3409
32. Wang X, Kulkarni SS, Tabarraei A (2019) Concurrent coupling of peridynamics and classical elasticity for elastodynamic problems. Comput Methods Appl Mech Eng 344:251–275
33. Pernatii A, Gabbert U, Naumenko K, Hesse J-T, Willberg C (2023) A penalty method for coupling of finite-element and peridynamic models. PAMM 22(1):035414
34. Pernatii A, Gabbert U, Hesse JT, Willberg C (2023) A fem-pd coupling based on Arlequin approach to impose boundary conditions in peridynamics. PAMM 23:e202300176
35. Qiang D, Li XH, Jianfeng L, Tian X (2018) A quasi-nonlocal coupling method for nonlocal and local diffusion models. SIAM J Numer Anal 56(3):1386–1404
36. Jiang F, Shen Y (2022) A quasi-nonlocal coupling method for bond-based peridynamics with classical continuum mechanics. Eng Comput 39(2):554–573
37. To AC, Li S (2005) Perfectly matched multiscale simulations. Phys Rev B 72(3):035414
38. Sun B, Li S, Quan G, Jinping O (2019) Coupling of peridynamics and numerical substructure method for modeling structures with local discontinuities. Comput Model Eng Sci 120(3):739–757
39. Reddy JN (1993) An introduction to the finite element method. McGraw-Hill Education, New York
40. Zienkiewicz OC, Taylor RL (2000) The finite element method: the basis, vol 1. Butterworth-Heinemann, Oxford, UK
41. Willberg C (2013) Development of a new isogeometric finite element and its application for Lamb wave based structural health monitoring. VDI Verlag, ISBN: 978-3-18-344620-9, Düsseldorf, fortschrit edition
42. Silling SA, Epton M, Olaf Weckner JX, Askari E (2007) Peridynamic states and constitutive modeling. J Elast 88:151–184
43. Silling SA, Askari E (2005) A meshfree method based on the peridynamic model of solid mechanics. Comput Struct 83(17–18):1526–1535
44. Madenci E, Oterkus E (2014) Peridynamic theory and its applications, vol 1. Springer, New York
45. Trageser J, Seleson P (2020) Bond-based peridynamics: a tale of two poisson's ratios. J Peridyn Nonlocal Model 2(3):278–288
46. Huang X, Bie Z, Wang L, Jin Y, Liu X, Guoshao S, He X (2019) Finite element method of bond-based peridynamics and its abaqus implementation. Eng Fract Mech 206:408–426
47. Graff K (1975) Wave motion in elastic solids. Dover Publications, New York
48. Achenbach JD (1975) Wave propagation in elastic solids. Elsevier, Amsterdam
49. Bažant ZP, Luo W, Chau VT, Bessa MA (2016) Wave dispersion and basic concepts of peridynamics compared to classical nonlocal damage models. J Appl Mech 83(11):111004
50. Bobaru F, Yang M, Alves LF, Silling SA, Askari E, Jifeng X (2009) Convergence, adaptive refinement, and scaling in 1d peridynamics. Int J Numer Meth Eng 77(6):852–877
51. Zhiyong Chen J, Woody J, Guoshao S, Huang X, Li S, Zhai L (2019) Influence of micro-modulus functions on peridynamics simulation of crack propagation and branching in brittle materials. Eng Fract Mech 216:106498
52. Naumenko K, Yang Z, Ma C-C, Chen Y (2023) Closed-form series solutions to peridynamic rod equations: influence of kernel function. Tech Mechanik - Eur J Eng Mech 43(2):259–270
53. Keyes DE (ed) (1997) Parallel numerical algorithms. ICASE / LaRC interdisciplinary series in science and engineering, vol 4. Springer, Dordrecht
54. Gander MJ (2006) Optimized Schwarz methods. SIAM J Numer Anal 44(2):699–731
55. Gander MJ (2008) Schwarz methods over the course of time. Electron Trans Numer Anal 31:228–255
56. Dhia HB (1998) The arlequin method: a partition of models for concurrent multiscale analyses. Comptes Rendus de l'Académie des Sciences, pages 1–3
57. Hashmi Ben Dhia and Guillaume Rateau (2005) The arlequin method as a flexible engineering design tool. Int J Numer Meth Eng 62(11):1442–1462
58. Gabbert U (1982) Berücksichtigung von zwangsbedingungen in der fem mittels der penalty-funktion-methode. Tech Mech 4(2):40–46
59. Zaccariotto M, Tomasi D, Galvanetto U (2017) An enhanced coupling of pd grids to fe meshes. Mech Res Commun 84:125–135
60. Ongaro G, Seleson P, Galvanetto U, Ni T, Zaccariotto M (2021) Overall equilibrium in the coupling of peridynamics and classical continuum mechanics. Comput Methods Appl Mech Eng 381:113515
61. D'Elia M, Li X, Seleson P, Tian X, Yu Y (2022) A review of local-to-nonlocal coupling methods in nonlocal diffusion and nonlocal mechanics. J Peridyn Nonlocal Model 4:1–50
62. Nishawala VV, Ostoja-Starzewski M (2017) Peristatic solutions for finite one- and two-dimensional systems. Math Mech Solids 22(8):1639–1653